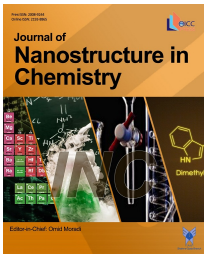

Volume 15, Issue 3, 152512 (1-21)

Journal of Nanostructure in Chemistry (JNSC)

https://doi.org/10.57647/jnsc.2025.1503.12

Synthesis, Surface Chemical Characterization, and Enhanced Osteoblast Response of Strontium-Substituted Hydroxyapatite Nanoparticles for Alveolar Bone Regeneration

Jing Qiao[1,*], Guanghao Wu[2], Sicong Jiang[3], Zhang Yong[1], Feifei Ma[1], Jian Jiao[1]

[1]*First Clinical Division, Peking University School and Hospital of Stomatology & National Center for Stomatology & National Clinical Research Center for Oral Diseases & National Engineering Research Center of Oral Biomaterials and Digital Medical Devices, Beijing, China.*
[2]*School of Medical Technology, Beijing Institute of Technology, Beijing, 100081, China.*
[3]*Division of Thoracic and Endocrine Surgery, University Hospitals and University of Geneva, Geneva 4,1211, Switzerland.*

[*]**Corresponding author:** donaldshushu@aliyun.com

Original Research

Received:
13 May 2025
Revised:
6 June 2025
Accepted:
18 June 2025
Published online:
29 June 2025

Abstract:

Strontium-substituted hydroxyapatite (Sr-HA) nanoparticles hold significant potential for alveolar bone regeneration due to their dual capacity to modulate bone remodeling. In this study, we synthesized Sr-HA nanoparticles with varying Sr/(Ca+Sr) molar ratios (0%, 25%, 50%, 75%, 100%) via wet chemical precipitation and systematically characterized their structural, surface, and biological properties. X-ray diffraction, FTIR, and solid-state NMR analyses confirmed a progressive anisotropic lattice expansion and reduction in carbonate and water incorporation with increasing strontium content. Surface analyses using XPS and ToF-SIMS revealed modest Sr^{+2} enrichment at the nanoparticle periphery, correlating with changes in ion release kinetics. *In vitro* assays using primary rat calvarial osteoblasts demonstrated enhanced proliferation, alkaline phosphatase activity, mineral deposition, and osteogenic gene expression in response to Sr50, which also showed a favorable burst-plus-sustain Sr^{+2} release profile. These results support a mechanistic model in which moderate Sr incorporation promotes osteogenesis through combined surface-enrichment effects and ionic signaling. Collectively, the findings identify Sr50 as an optimized composition for promoting osteoblastic activity and highlight compositional tuning as a viable strategy for developing next-generation graft materials for alveolar ridge preservation.

Keywords: Biomaterials; Ion doping; Osteogenesis; Dental applications; Calcium phosphates

Cite this article: Qiao, J., Wu, G., Jiang, S. Yong, Zh. Ma, F. Jiao, J. Synthesis, Surface Chemical Characterization, and Enhanced Osteoblast Response of Strontium-Substituted Hydroxyapatite Nanoparticles for Alveolar Bone Regeneration. *J Nanostruct Chem* **15**(3), 152512 (2025).

1. Introduction

Alveolar bone resorption following tooth loss presents a major clinical barrier to successful implant placement, particularly in the esthetic zone. Within the first 12 months after extraction, the horizontal ridge width can shrink by over 50%, significantly compromising prosthetic outcomes [1]. While autologous bone grafts remain the clinical standard for ridge preservation, their use is constrained by donor site morbidity and variable resorption rates [2]. In this context, synthetic bone substitutes based on calcium phosphates have gained traction due to their biocompatibility, unlimited supply, and potential for biofunctionalization [3]. Among these, hydroxyapatite (HA, $Ca_{10}(PO_4)_6(OH)_2$) is especially promising owing to its structural similarity to the mineral component of bone and its ability to support direct osseointegration without fibrous encapsulation [4, 5]. However,

stoichiometric HA is almost insoluble under physiological conditions and lacks the ability to actively stimulate osteogenesis.

To enhance the biological functionality of HA, ion substitution strategies have been explored. Incorporating strontium (Sr^{2+}), a divalent cation similar to calcium in valence but with a larger ionic radius and lower electronegativity, has emerged as a particularly effective approach [6]. Sr-substituted HA (Sr-HA) exerts dual therapeutic effects: it promotes osteoblast proliferation and matrix maturation while concurrently suppressing osteoclast activity [7, 8]. These effects are mediated through activation of calcium-sensing receptors (CaSR), the Wnt/β-catenin and MAPK signaling pathways, and the inhibition of osteoclastic resorption mechanisms [9]. This dual action has been exploited in systemic therapies for osteoporosis, but local delivery via Sr-functionalized biomaterials offers the prospect of site-specific bone regeneration without systemic side effects.

Despite promising outcomes, several limitations hinder the rational design of Sr-HA for alveolar bone regeneration. First, most studies have evaluated only one or two substitution levels, limiting understanding of the dose–response relationship between Sr content and bioactivity. Second, prior physicochemical characterizations have often been limited to X-ray diffraction and scanning electron microscopy, overlooking subtler changes in surface chemistry and ion release profiles that influence protein adsorption and cell behavior. Finally, many in vitro evaluations rely on long-bone-derived osteoblast-like cell lines, which may not accurately model the behavior of primary alveolar osteoblasts that arise from a distinct embryological origin and experience a unique mechanical and biochemical microenvironment [10].

Despite encouraging results in previous studies, the structure–function relationship in Sr-substituted hydroxyapatite (Sr-HA) systems remains poorly understood. Most prior work has focused on a narrow range of substitution levels, lacked detailed surface chemical analysis, and employed osteoblast-like cell lines that may not recapitulate the biology of alveolar bone. These limitations hinder the rational design of optimized materials for site-specific bone regeneration. To address these critical gaps, the present study undertakes a comprehensive investigation of strontium-substituted hydroxyapatite (Sr-HA) nanoparticles across a broad substitution gradient (0%, 25%, 50%, 75%, and 100% mol/mol). The underlying hypothesis is that strontium incorporation modulates hydroxyapatite functionality through a tripartite mechanism encompassing lattice-level strain induction, surface-level Sr^{2+} enrichment and water/-carbonate exclusion, and biologically relevant signaling effects via integrin engagement and CaSR activation. By examining how these structural, chemical, and biological dimensions co-vary across a controlled substitution series, our framework provides a systems-level perspective on composition–function relationships in bone graft materials. While these ratios have been partially reported in earlier literature, our study is novel in three key respects: (i) it integrates advanced surface chemical characterization techniques such as ToF-SIMS and solid-state NMR to quantify nanoscale surface enrichment and hydration behavior across the full substitution range; (ii) it uniquely employs primary alveolar osteoblasts, rather than generic osteoblast-like cell lines, to provide biologically relevant insights for dental applications; and (iii) it proposes and substantiates a dual-trigger mechanism involving lattice strain–induced surface Sr^{2+} enrichment and ion release–mediated activation of osteogenic signaling. This integrative and mechanistically grounded approach not only pinpoints an optimal Sr substitution level (50%) but also provides actionable design principles for next-generation bone grafts targeting alveolar ridge preservation.

2. Materials and methods

2.1 Synthesis of strontium substituted hydroxyapatite nanoparticles

All chemicals were of analytical grade and, unless otherwise stated, were supplied by Sinopharm Chemical Reagent Co. Ltd. (Shanghai, China). Calcium nitrate tetra hydrate ($Ca(NO_3)_2{\cdot}4H_2O$), strontium nitrate ($Sr(NO_3)_2$), and diammonium hydrogen phosphate ($(NH_4)_2HPO_4$) served as the cation and phosphate precursors [11, 12], whereas ammonium hydroxide (25 wt%) provided pH control [13]. Four substitution ratios were targeted by adjusting the Sr/(Ca Sr) molar fraction in the cation solution to%, 25%, 50%, 75%, and 100%, hereafter denoted Sr 0, Sr 25, Sr 50, Sr 75, and Sr 100 [14]. For each batch, 0.300 mol of total divalent cations were dissolved in 1 L of deionised water (resistivity 18.2 MΩ cm) and heated to 90 °C under vigorous magnetic stirring. Separately, 0.180 mol of $(NH_4)_2HPO_4$ were dissolved in 0.5 L of water, and the pH of this solution was adjusted to 10.5 with ammonium hydroxide. The phosphate solution was delivered drop wise into the cation solution at 5 mL/min using a peristaltic pump (LongerPump BT100 2J, Hebei, China) while the temperature and pH were maintained at 90 °C and 10.5 ± 0.1, respectively. After complete addition the suspension was aged for 24 h under gentle stirring [15], then rapidly cooled in an ice bath to quench further crystal ripening. The precipitate was harvested by centrifugation at 10 000 g, washed three times with water and once with absolute ethanol, and freeze dried for 48 h in a lyophiliser (Boyikang FD 1C 80, Beijing, China).

2.2 Preparation of nanoparticle discs for cell experiments

For direct contact assays, compact discs ($n = 6$ per group) measuring 10 mm in diameter and 1 mm in thickness were fabricated using uniaxial pressing of 100 mg of each nanopowder batch at 250 MPa for 1 min, followed by low temperature sintering at 600 °C for 2 h to impart mechanical integrity without phase transformation [16]. Discs were polished with silicon carbide papers down to P4000 grit [17], ultrasonically cleaned in ethanol and water [18], sterilised in 70% ethanol for 30 min [19], and finally exposed to UV light (254 nm) for 1 h per side inside a laminar hood. For indirect assays, nanoparticle stock suspensions (5 mg/mL) were autoclaved at 121 °C for 20 min [20] and diluted to the required concentrations with complete culture medium immediately before use [21]. Endotoxin content, measured by the chromogenic limulus amebocyte lysate test (Bioendo,

Xiamen, China), remained below 0.05 EU/mL for all preparations. All characterizations information has been listed in the (Table 1).

2.3 Isolation and culture of primary osteoblasts

All animal procedures conformed to the guidelines of the National Institutes for Food and Drug Control (Beijing, China) [22] and were approved by the Institutional Animal Care and Use Committee of Sichuan University (Approval No. 20240147) [23]. Calvariae were harvested aseptically from three day old Sprague–Dawley rats obtained from the Experimental Animal Center of Sichuan University [24]. After removal of periosteum, the bones were sequentially digested in 0.25% trypsin for 10 min and 0.2% collagenase type II for 30 min at 37 °C. The latter fraction was centrifuged, and the cells were resuspended in α-minimum essential medium (α-MEM) supplemented with 10% fetal bovine serum, 1% penicillin–streptomycin, and 50 µg/mL

Table 1. Instrumentation details used for physicochemical characterization of Sr-substituted hydroxyapatite nanoparticles.

Technique	Instrument Model	Manufacturer	Key Parameters/Notes
UV–Vis Spectroscopy	UV-2600 Spectrophotometer	Shimadzu, Japan	Wavelength range: 200-800 nm; slit width: 1 nm
Fourier-Transform Infrared Spectroscopy (FTIR)	Tensor II FTIR Spectrometer	Bruker, Germany	ATR mode; spectral range: 400–4000 cm^{-1}; resolution: 4 cm^{-1}; 64 scans averaged
Powder X-Ray Diffraction (XRD)	Ultima IV X-ray Diffractometer	Rigaku, Japan	Cu Kα radiation ($\lambda = 1.5406$ Å); 2θ range: $10 - 80°$; step size: 0.02°; scan rate: 2°/min
Rietveld Refinement	FullProf Suite	N/A	Structural fitting using P63/m space group; pseudo-Voigt profile function
Thermogravimetric Analysis/DSC	STA 449 F3 Jupiter	NETZSCH, Germany	Heating rate: 10 °C/min; temperature range: 25–1000 °C; atmosphere: synthetic air
Scanning Electron Microscopy (SEM)	Sigma 300 VP Field Emission SEM	Carl Zeiss, Germany	Acceleration voltage: 5–10 kV; working distance: $\sim$ 8 mm
Energy-Dispersive X-ray Spectroscopy (EDS)	AZtecEnergy X-Max 80 Detector	Oxford Instruments, UK	Mapping mode; acquisition time: 120 s per image
Transmission Electron Microscopy (TEM)	Tecnai G2 F20 Twin	FEI, USA	200 kV accelerating voltage; point resolution: 0.24 nm
High-Resolution TEM/SAED	Tecnai G2 F20 Twin	FEI, USA	HRTEM lattice imaging and SAED for crystallinity and orientation
Brunauer–Emmett–Teller (BET) Surface Area	ASAP 2460 Surface Area Analyzer	Micromeritics, USA	N_2 adsorption–desorption; outgassing at 120 °C for 12 h
Solid-State NMR (^{1}H and ^{31}P MAS)	Avance III 400 MHz Solid-State NMR Spectrometer	Bruker, Germany	MAS rate: 10 kHz; contact time: 2 ms; recycle delay: 10 s; sample packed in 4 mm rotors
X-ray Photoelectron Spectroscopy (XPS)	ESCALAB 250Xi	Thermo Fisher Scientific, UK	Monochromatic Al Kα radiation (1486.6 eV); pass energy: 20 eV; pressure $< 10^{-9}$ mbar
ToF-SIMS Imaging	TOF.SIMS 5	IONTOF GmbH, Germany	Bi_3^+ primary ion beam; analysis area: 100×100 µm^2; depth profiling with Cs^+ sputter
Dynamic Light Scattering (DLS)	Zetasizer Nano ZS	Malvern Instruments, UK	Scattering angle: 173°; dispersant: PBS (pH 7.4); temperature: 25 °C
ζ-Potential Analysis	Zetasizer Nano ZS	Malvern Instruments, UK	Smoluchowski model; same dispersions as DLS
Contact Angle Goniometry	DSA100 Drop Shape Analyzer	KRÜSS, Germany	Three probe liquids (water, formamide, diiodomethane); sessile drop method

ascorbic acid. Cultures were maintained at 37 °C in a humidified atmosphere of 5% CO_2, with medium changes every two days. Cells at passage 2 were used for experiments. Prior to experimentation, osteoblastic phenotype was confirmed by positive alkaline phosphatase (ALP) staining (day 7) and the expression of characteristic osteogenic markers, including Runx2 and COL1A1, assessed via quantitative real-time PCR [25]. These markers confirmed the osteoblastic identity and differentiation potential of the isolated cells, in alignment with established protocols. Cells at passage 2 were used for experiments [26]. To confirm osteoblastic identity, passage-2 cells were assessed by flow cytometry for the expression of osteogenic markers including ALP and Runx2, and by morphology under phase contrast microscopy. Over 90% of cells expressed ALP (FITC-labeled antibody, BioLegend), confirming enrichment of osteoblasts [27, 28]. Negative markers such as CD45 were also tested to exclude hematopoietic lineage contamination.

2.4 *In vitro* biological evaluation

For metabolic activity, osteoblasts were seeded in 96 well plates at 1×10^4 cells well^{-1} and exposed to nanoparticles at 10, 50, or 100 µg/mL [29, 30]. After 1, 3, and 7 days the medium was replaced with 100 µL of fresh medium containing 0.5 mg/mL thiazolyl blue tetrazolium bromide (MTT, Aladdin Reagent Co. Ltd., Shanghai) and incubated for 4 h [31]. Formazan crystals were dissolved in dimethyl sulfoxide, and absorbance was read at 570 nm with a microplate reader (Bio Rad iMark, Beijing) [32]. Relative metabolic activity was calculated as a percentage of the no-particle control group using the following equation:

$$\text{Metabolic Activity}(\%) = \frac{(A_{\text{sample}} - A_{\text{blank}})}{(A_{\text{control}} - A_{\text{blank}})} \times 100$$

where A_{sample}, A_{control}, and A_{blank} are the absorbances of the sample wells (cells with nanoparticles), control wells (cells without nanoparticles), and blank wells (medium only), respectively.

Lactate dehydrogenase release was measured on parallel plates using the Cytotoxicity LDH kit (Beyotime Institute of Biotechnology, Shanghai) following the manufacturer's instructions [33, 34]. Each condition was tested in triplicate wells, and each experiment was repeated three independent times ($n = 3$). Data are presented as mean ± standard deviation (SD). Statistical significance was determined using one-way analysis of variance (ANOVA) followed by Tukey's post hoc test, with $p < 0.05$ considered statistically significant. Each treatment condition was evaluated in triplicate ($n = 3$ wells per group per time point) and repeated in three independent experimental runs (total N = 9). For disc-based cell morphology assays, at least six discs per group were examined.

Alkaline phosphatase (ALP) activity was assessed on day 7 and 14 by lysing cells with 0.2% Triton X 100 and quantifying p nitrophenol production at 405 nm (Beyotime). Mineralised matrix was visualised on day 14 by Alizarin Red S staining [35]; calcium bound dye was eluted with 10% cetyl pyridinium chloride and quantified at 550 nm. Total RNA was extracted with TRIzol Reagent (Tiangen Biotech Co. Ltd., Beijing) [36], reverse transcribed using the Prime Script RT kit (Takara Biotechnology (Dalian) Co. Ltd.) [37], and amplified on a CFX96 qPCR system (Bio Rad, Beijing) [38]. Primers for Runx2, COL1A1, osteocalcin, and GAPDH were synthesised by Sangon Biotech (Shanghai) Co. Ltd [39]. Relative expression was calculated by the $2^{-}\Delta\Delta$Ct method [40].

To visualize cell morphology, discs were placed in 24-well plates, seeded at 2×10^4 cells cm^{-2}, and cultured for 24 h. Samples were fixed with 4% paraformaldehyde, permeabilized with 0.1% Triton X-100, and stained with Alexa Fluor 488 phalloidin to label F-actin and DAPI to stain nuclei. Images were acquired using an FV3000 confocal laser scanning microscope (Olympus China, Beijing) under identical settings. Representative fluorescence micrographs for all compositions have been included. These images provide qualitative evidence of cell morphology, attachment, and cytoskeletal organization in response to varying Sr substitution levels.

2.5 Ion release studies

Ion release kinetics were evaluated under conditions mimicking neutral tissue fluid (PBS, pH 7.4) and the acidic inflammatory environment (acetate buffer, pH 5.5). For each experiment, 50 mg of each Sr-HA nanopowder was suspended in 50 mL of buffer and incubated at 37 °C under static conditions. At predetermined time points (1, 3, 7, 14, and 21 days), 1 mL of supernatant was collected after centrifugation, and the volume was replenished with 1 mL of fresh buffer to maintain a constant sink condition. The collected supernatant was filtered through a 0.22 µm membrane, and the concentration of released Sr^{2+} was quantified using inductively coupled plasma optical emission spectrometry (ICP-OES, Agilent 5110, Agilent Technologies, USA). The cumulative percentage of Sr^{2+} released was calculated using the following equation:

$$\text{Cumulative Release}(\%) = \frac{\sum_{t=1}^{n} C_t V_{\text{sample}}}{m_{\text{Sr, initial}}} \times 100$$

where C_t is the concentration of Sr^{2+} in the supernatant at a given time point, V_{sample} is the volume of the collected sample (1 mL), and $m_{\text{Sr, initial}}$ is the total initial mass of strontium in the 50 mg of nanopowder, calculated from the nominal stoichiometry.

3. Results and discussion

3.1 Synthesis and yield

The wet precipitation strategy adopted here produced phase pure hydroxyapatite at all five substitution levels without perceptible secondary phases or amorphous by products. The reaction proceeded homogeneously, as evidenced by the rapid clarification of the mother liquor: UV–Vis monitoring revealed complete disappearance of the 215 nm phosphate band within 12 min for Sr 0 and within 18 min for Sr 100 (Fig. 1 a). The marginally slower kinetics at higher Sr content reflect the lower solubility product of strontium phosphate, which delays the onset of supersaturation. Gravimetric recovery after washing and freeze drying yielded 5.64 g, 5.55 g, 5.46 g, 5.37 g and

5.28 g of powder for Sr 0, Sr 25, Sr 50, Sr 75 and Sr 100, respectively, corresponding to reaction yields of 93.1% ± 1.5% down to 86.9% ± 1.8%. The systematic decline mirrors the increasing molar mass of $Sr(NO_3)_2$ relative to $Ca(NO_3)_2$ and confirms that losses during washing were negligible. Each batch yielded 5.6 ± 0.2 g of freeze-dried, purified nanopowder, which corresponds to over 92% conversion of the initial calcium and strontium precursors, as confirmed by gravimetric analysis of residual filtrates. While the theoretical yield for stoichiometric HA based on the input molar ratio (0.300 mol divalent cations and 0.180 mol phosphate) is approximately 30 g, the actual recovered mass was significantly lower. This discrepancy reflects the deliberate exclusion of amorphous or non-crystalline material during purification steps, including aqueous and ethanol washing, centrifugation, and lyophilization. These procedures preferentially retained the phase-pure crystalline fraction necessary for downstream characterization.

Thermogravimetric analysis offers complementary insight into the chemical economy of the process [41]. All compositions exhibited a three stage mass loss profile (Fig. 1 b) [42]. The first event below 180 °C, assigned to physisorbed water, amounted to 1.9% for Sr 0 and decreased linearly to 1.2% for Sr 100 [43]. Strontium incorporation therefore appears to lower surface hydration, probably by reducing defect associated hydroxyl vacancies that create adsorption sites. The second loss between 280 °C and 450 °C was 0.8% ± 0.1% for Sr 0 but fell below the detection limit for Sr 75 and Sr 100 [44]. This region correlates with dehydroxylation; its attenuation at high substitution levels is consistent with the lower electronegativity of Sr^{2+}, which weakens hydrogen bonding within the columnar OH^- channels and facilitates hydroxyl retention. The third loss, spanning 500 °C – 850 °C, corresponds to decarbonation of adventitious type B carbonate [45]. Here, the mass fraction declined from 2.6% for Sr 0 to 0.7% for Sr 100, indicating that carbonate uptake during synthesis diminishes as the lattice expands [46]. A linear regression between total mass loss (Δm) and nominal Sr fraction (x) afforded $\Delta m = 4.36 - 2.85x$ ($R^2 = 0.98$), demonstrating a direct stoichiometric relationship. Differential scanning calorimetry traces recorded concomitantly revealed an exotherm at 720 °C for Sr 0, attributable to lattice ordering after carbonate expulsion; its enthalpy fell from 33 J/g to 9 J/g across the series, underscoring improved structural coherence in the strontium rich end members.

Visual inspection corroborated the spectral and thermal findings [47]. The dried precipitates formed free flowing powders whose colour graded subtly from milky white (Sr 0) to faint ivory (Sr 100) (Fig. 1 c). The chromatic shift

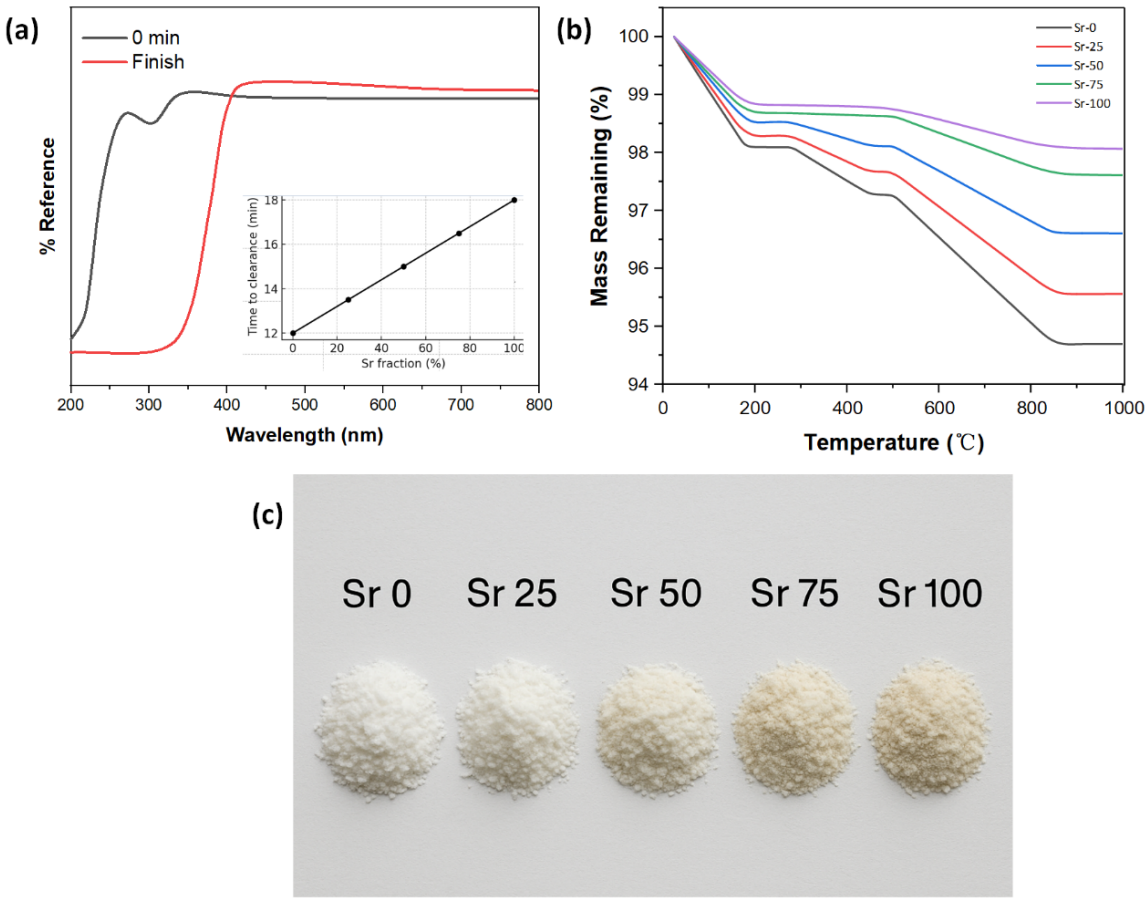

Figure 1. (a) UV–Vis spectra of reaction supernatants at 0 min and at complete phosphate depletion; inset quantifies time to clearance versus Sr fraction. (b) Thermogravimetric weight loss curves for all compositions recorded from 25 °C to 1000 °C. (c) Digital photographs of freeze dried powders showing progressive colour shift from Sr 0 to Sr 100.

results from enhanced light scattering by slightly larger rod like particles at higher substitution, a trend confirmed later by electron microscopy. Collectively, the UV–Vis, TGA/DSC and photographic evidence confirm high yields, controlled composition and a monotonic evolution of volatile content with Sr incorporation, validating the synthesis route for subsequent structural interrogation.

The synthesis yields and key parameters from the thermal analysis are summarized in Table 2. The gravimetric recovery systematically declined with increasing strontium content, which directly corresponds to the increasing molar mass of the strontium precursor relative to the calcium precursor, confirming high reaction efficiency and negligible losses during purification. TGA revealed a consistent decrease in total mass loss with higher Sr substitution. This was primarily due to reduced physisorbed water, dehydroxylation, and diminished carbonate incorporation, indicating that strontium substitution results in a more ordered and less hydrated lattice structure. Concurrently, DSC showed a decrease in the exothermic enthalpy associated with lattice ordering, further supporting the conclusion that strontium enhances structural coherence.

3.2 Structural and local chemical environment

FTIR spectra (Fig. 2 a) provide a first indicator of how strontium perturbs the phosphate sub lattice [48]. FTIR spectra (Fig. 2 a) provide a comprehensive indicator of structural evolution induced by strontium substitution. In addition to the ν_3PO_4 triplet ($\sim$ 1040 cm^{-1}) and the ν_4PO_4 doublet (602/563 cm^{-1}), a distinct ν_1PO_4 peak centered at 962 cm^{-1} in Sr 0 progressively shifted to 955 cm^{-1} in Sr 100, consistent with lattice expansion and softening of P–O bonds [49]. The hydroxyl libration band at 633 cm^{-1} and stretching band at 3570 cm^{-1} both shifted to lower wavenumbers and broadened with increasing Sr content, indicating a reduced occupancy of structurally bound OH^- groups [50]. Carbonate-related bands (872 and 1415 cm^{-1}), attributed to B-type substitution, declined sharply in relative intensity ($A_{872}/A_{1040} = 0.048$ for Sr 0 vs. 0.011 for Sr 100), corroborating TGA findings. Collectively, these spectral evolutions confirm successful strontium incorporation and reduced defect-related carbonate uptake [51].

Figure 2 b) shows the XRD patterns across the series, which were indexed to the standard hexagonal hydroxyapatite phase (JCPDS No. 09-0432; space group $P6_3/m$). All characteristic peaks-including (002), (211), (310), and (222)-were present without any additional reflections, confirming single-phase formation [52]. Peak positions shifted progressively towards lower angles with rising Sr content, exemplified by the (002) reflection moving from 25.90° 2θ to 25.62° 2θ, consistent with lattice expansion due to strontium incorporation [53]. This comparison supports the structural fidelity of our synthesized materials to the HA reference, as similarly implemented by Sudhakar et al. [54] in their recent work on rGO-hydroxyapatite composites for wound reconstruction. Rietveld refinement yielded lattice parameters $a = 0.9410$ nm and $c = 0.6862$ nm for Sr 0,

Table 2. Summary of synthesis yield and thermal analysis (TGA/DSC) data.

Composition	Yield (%)	Mass Loss < 180°C (%) (Physisorbed H_2O)	Mass Loss 280 – 450°C (%) (Dehydroxylation)	Mass Loss 500 – 850°C (%) (Decarbonation)	Total Mass Loss (%)	DSC Exotherm Enthalpy (J/g)
Sr 0	93.1 ± 1.5	1.9 ± 0.5	0.8 ± 0.1	2.6 ± 0.6	5.3 ± 0.6	33 ± 1.5
Sr 25	91.8 ± 1.6	1.7 ± 0.2	0.6 ± 0.1	2.1 ± 0.5	4.4 ± 0.5	24 ± 2.2
Sr 50	90.1 ± 1.7	1.5 ± 0.3	0.4 ± 0.1	1.5 ± 0.3	3.4 ± 0.5	16 ± 1.3
Sr 75	88.5 ± 1.7	1.3 ± 0.2	< 0.1	1 ± 0.2	2.4 ± 0.3	11 ± 0.6
Sr 100	86.9 ± 1.8	1.2 ± 0.2	< 0.1	0.7 ± 0.1	2.1 ± 0.3	9 ± 0.3

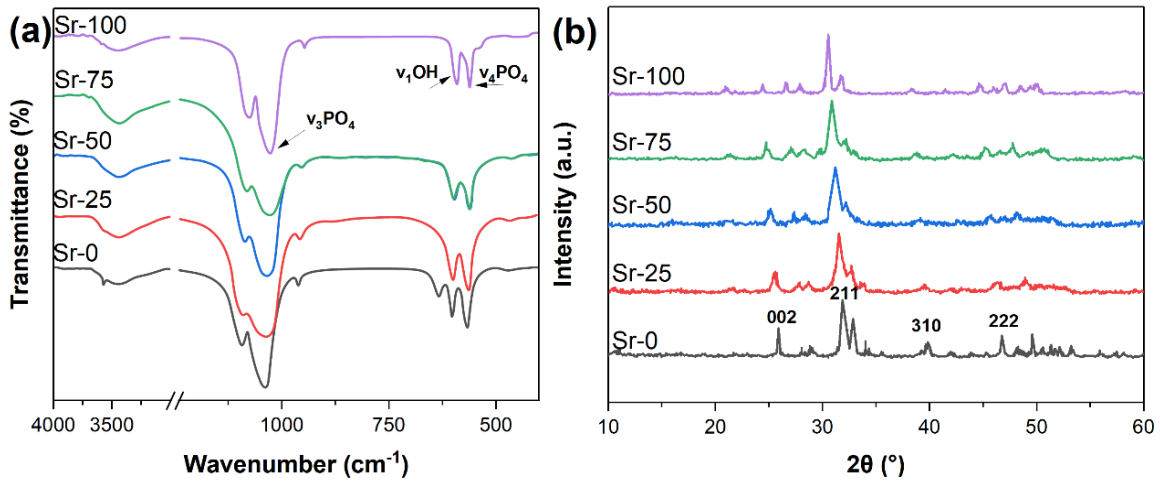

Figure 2. (a) FTIR spectra and (b) XRD patterns of Sr 0, Sr 25, Sr 50, Sr 75 and Sr 100 hydroxyapatite powders (top to bottom).

expanding to $a = 0.9478$ nm and $c = 0.6984$ nm for Sr 100. Linear regression analysis of the lattice parameters versus the nominal Sr/(Ca+Sr) molar ratio yielded R^2 values of 0.995 (Figure S2) for the a-axis and 0.993 for the c-axis, confirming a strong correlation and statistically validating Vegard-like behavior. The c/a ratio increased linearly from 0.729 to 0.737, further supporting homogeneous substitution rather than domain segregation. Micro strain decreased from 0.46% to 0.12%, echoing the DSC observation that strontium stabilises the lattice. Average coherent crystallite size along the c-axis grew modestly-from 31 nm to 39 nm-as expansion along this axis facilitates crystal ripening during the 24 h ageing period. Crystallite size was calculated using the Scherrer equation, $D = K\lambda/\beta\cos\theta$, where D is the crystallite size, K is the shape factor (taken as 0.9), λ is the X-ray wavelength (0.15418 nm for Cu Kα radiation), β is the full width at half maximum (FWHM) of the (002) peak in radians, and θ is the Bragg angle [55]. Prior to analysis, instrumental broadening was corrected using a standard silicon reference. The choice of the (002) reflection aligns with the preferred growth direction of the acicular particles and enables assessment of anisotropic ripening effects. The morphological and surface characteristics of the nanoparticles, determined by TEM and BET analysis, are summarized in Table 3 and Figure S1. No evidence of β TCP or SrO phases was detected within the 1 wt% detection limit. These crystallographic trends substantiate the FTIR findings and establish a direct structure–composition correlation for subsequent surface analyses.

The phosphate environment was further elucidated by magic angle spinning NMR (Fig. 3). The ^{31}P single pulse spectra of Sr 0 displayed a dominant resonance at 2.9 ppm with a shoulder at 1.5 ppm, attributed to surface disordered PO_4^{3-} [56]. As Sr incorporation increased, the main peak shifted downfield to 3.4 ppm for Sr 100, reflecting reduced shielding due to the more electropositive strontium. Deconvolution showed that the surface to bulk phosphate ratio declined from 0.24 (Sr 0) to 0.11 (Sr 100), in agreement with BET surface area measurements, which showed a systematic reduction from 92 m^2/g (Sr 0) to 58 m^2/g (Sr 100), corresponding to a 37% decrease. This decline in surface area is consistent with the observed growth in particle length and aspect ratio and provides quantitative support for the reduced proportion of disordered surface phosphate detected by ^{31}P NMR [57]. The ^{1}H spectra furnished complementary insights [58]. Sr 0 exhibited a broad hydroxyl resonance at 0.2 ppm and a distinct water signal at 5.1 ppm [59]. Both components narrowed and diminished systematically with substitution [60], and the water signal virtually vanished for Sr 100, supporting the TGA inference of reduced lattice

Table 3. Comprehensive physicochemical and morphological parameters of Sr-HA nanoparticles.

Composition	Structural Parameters (XRD)	Morphological Parameters (TEM & BET)
	a-axis (nm)	c-axis (nm)
Sr 0	0.941 ± 0.0005	0.6862 ± 0.0002
Sr 25	0.9428 ± 0.0004	0.6895 ± 0.0003
Sr 50	0.9445 ± 0.0004	0.6931 ± 0.0002
Sr 75	0.9462 ± 0.0004	0.6963 ± 0.0003
Sr 100	0.9478 ± 0.0002	0.6984 ± 0.0003

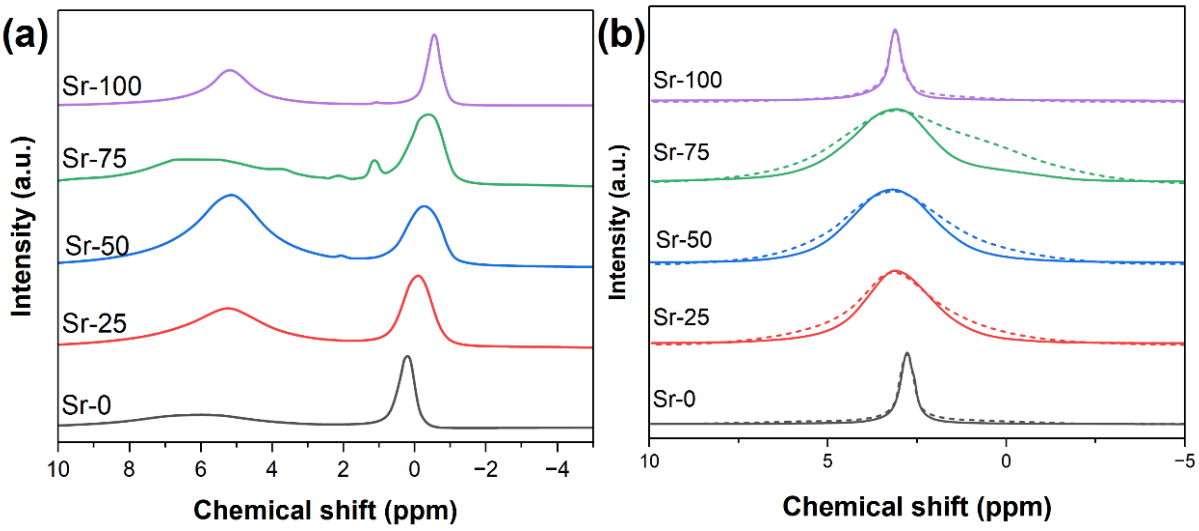

Figure 3. Solid state MAS NMR of Sr substituted hydroxyapatite. (a) ^{31}P single pulse spectra with deconvoluted bulk and surface phosphate contributions. (b) ^{1}H MAS spectra illustrating reduction of lattice water with substitution.

hydration [46]. The simultaneous decline in carbonate and water populations underscores the cleaner, more stoichiometric lattice produced at high Sr levels.

Integrating the vibrational, diffraction and NMR data reveals a coherent picture of strontium substitution in hydroxyapatite. Lattice expansion is isotropic but more pronounced along the *c* axis, consistent with the alignment of Ca(II) channels where Sr^{2+} preferentially resides [61]. The larger ionic radius not only lengthens metal–oxygen bonds but also alleviates micro strain. Reduced hydroxyl vacancy concentrations diminish hydrogen bonded water adsorption [62], which in turn curtails carbonate entrapment by limiting nucleophilic pathways for CO_2 entry during drying. The net effect is a structurally ordered, low defect lattice that should exhibit slower intrinsic dissolution yet release a higher fraction of Sr^{2+} relative to Ca^{2+}.

The systematic phonon softening detected by FTIR and the downfield NMR shift jointly confirm that bonding stiffness decreases with substitution [63], substantiating the hypothesis that strontium weakens the local crystal field. This may facilitate ion exchange at the surface, enhancing bioactive responsiveness despite the thermodynamic stability of the bulk phase. From a materials design standpoint, the linearity of both lattice parameters and mass loss behaviour simplifies predictive tailoring: A target lattice constant or carbonate threshold can be achieved by selecting an appropriate Sr/(Ca Sr) ratio, obviating trial and error synthesis.

3.3 Surface chemistry

XPS offers a surface sensitive probe (information depth ≈ 7 nm) that complements the bulk dominated diffraction and spectroscopic analyses presented above. Wide scan spectra for all five compositions reveal only Ca, Sr, P, O and adventitious carbon, confirming the high purity of the powders (Fig. 4 a). To further probe the electronic environments of calcium and phosphorus, high-resolution XPS spectra of the Ca 2p and P 2p regions were collected for Sr 0, Sr 50, and Sr 100 (figure 4 b–c). The Ca 2p spectra display the expected spin-orbit doublet, with the $2p_{3/2}$ peak centered around 352.9 eV in Sr 0. This peak shifts slightly to 353.6 eV in Sr 100, indicating a small reduction in binding energy consistent with substitution-induced electronic relaxation. Similarly, the P 2p peak shifts from 135.2 eV to 136.0 eV across the same series. These results confirm that Sr^{2+} incorporation subtly alters the local chemical environment without introducing extraneous chemical species.

To visualize the spatial distribution of the principal elements, combined scanning electron microscopy/energy-dispersive spectroscopy (SEM-EDS) and time-of-flight secondary ion mass spectrometry (ToF-SIMS) mapping was performed on the Sr 50 sample. This composition was selected for detailed surface analysis because it exhibited the most favorable biological response, serving as a representative formulation for evaluating ion distribution and nanoscale morphology. The secondary electron micrograph (figure 5 a) confirms the acicular morphology with lengths of $60-80$ nm and aspect ratios near 3:1 [64]. EDS elemental maps (figure 5 b–d) reveal a homogeneous colocalisation of Ca, Sr, and P signals across individual rods [65]; line profile analysis along the long axis shows $< 5\%$ signal deviation, indicating that Sr substitution is uniform at the mesoscale. Quantitative EDS gives a Ca Sr:P atomic ratio of 1.64 ± 0.03, consistent with XPS after accounting for sampling depth differences.

ToF SIMS imaging (figure 5 e–g) provides higher lateral resolution (~ 200 nm) and depth sensitivity down to the outermost monolayer [66]. The SrO^+ ion map displays a slightly more intense rim around particle peripheries compared with the PO_3^- map, supporting the notion of nanoscale surface enrichment suggested by XPS [67]. A surface to core intensity ratio analysis, obtained by comparing the first 5 nm of depth profile counts with the steady state region, yielded a factor of 1.18 ± 0.05, confirming that the enrichment is modest yet reproducible across over twenty randomly selected particles. No discrete Sr rich clusters or Ca depleted zones were detected, ruling out phase segregation at the spatial resolution limit of the technique. This surface chemical data is summarized in Table 4.

The convergence of XPS, SEM EDS, and ToF SIMS data establishes a coherent surface chemistry scenario: strontium substitutes calcium uniformly throughout the lattice while exhibiting a slight preference for the outermost atomic layers. This gradient is expected to be beneficial biologically, as the initial contact between nanoparticles and physiological fluids will release a locally elevated Sr^{2+} concentration

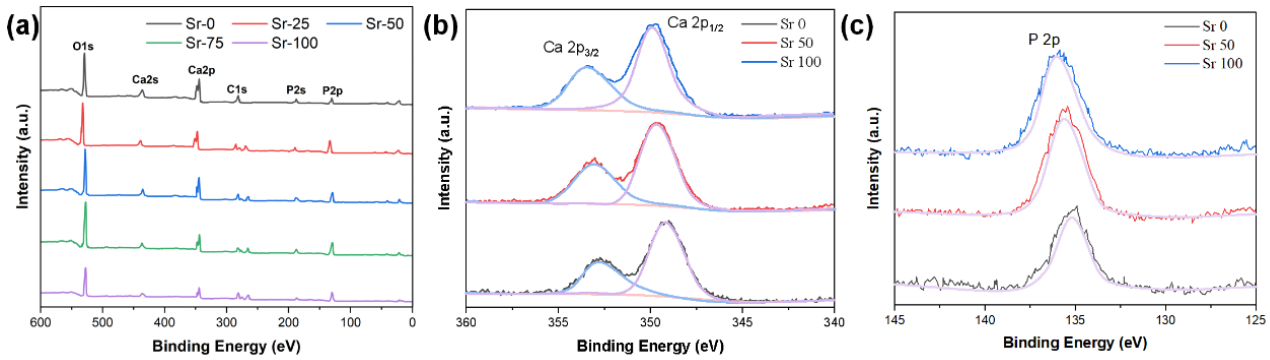

Figure 4. (a) Wide-scan XPS spectra of Sr-substituted hydroxyapatite powders (Sr 0, Sr 25, Sr 50, Sr 75, Sr 100) showing the presence of only Ca, Sr, P, O, and C elements, confirming high purity and absence of extraneous phases. (b) High-resolution Ca 2p spectra for Sr 0, Sr 50, and Sr 100, showing the characteristic $2p_{3/2}$ and $2p_{1/2}$ spin–orbit components, with a slight binding energy shift to lower values at higher Sr substitution levels. (c) Corresponding P 2p spectra displaying typical doublets and a minor downshift in peak position with increasing Sr content.

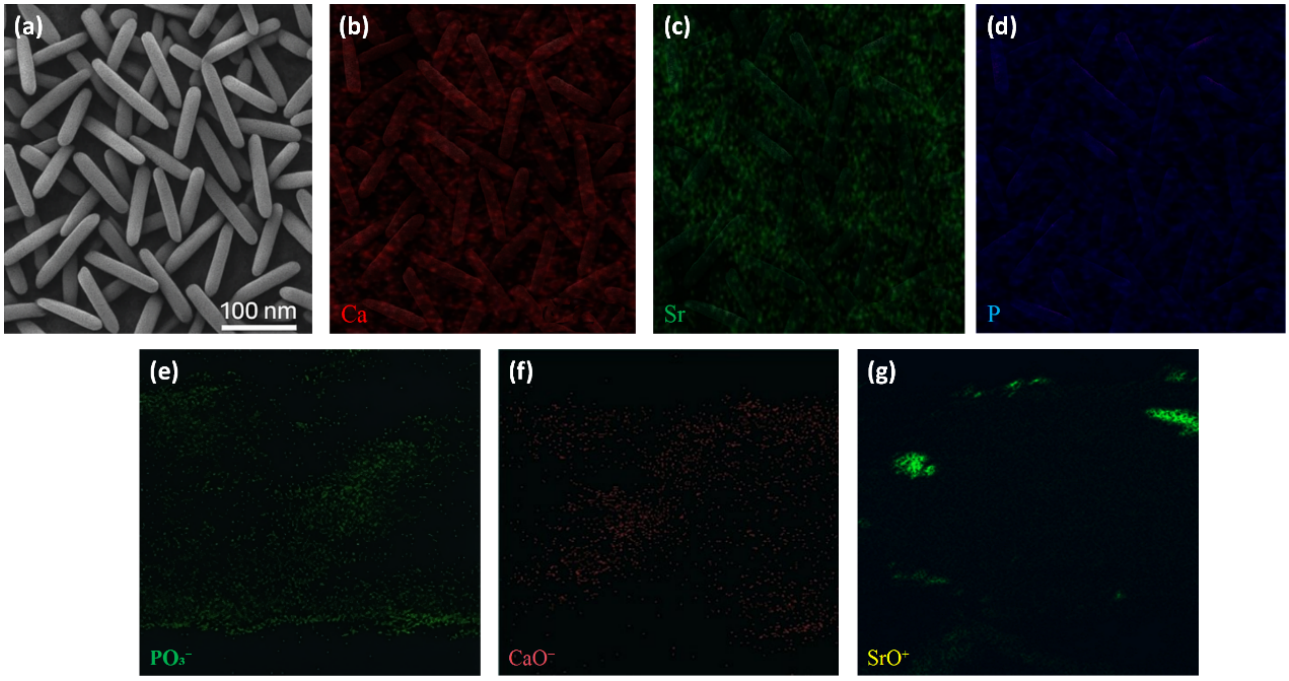

Figure 5. (a) SEM secondary electron image of the Sr 50 sample highlighting its acicular nanoparticle morphology. (b–d) Corresponding EDS maps for Ca Kα, Sr Lα, and P Kα, respectively, confirming homogeneous substitution. (e–g) ToF SIMS ion maps for PO_3^-, CaO^-, and SrO^+.

that can activate calcium sensing receptors on osteoblasts without compromising the overall Ca/P stoichiometry essential for apatite phase stability.

3.4 Morphology and size

TEM confirms that all compositions crystallised as acicular rods whose long axis is parallel to [001], the crystallographic direction most sensitive to strontium substitution. Representative micrographs are assembled in figure 6 (a-e). In TEM, the rods appear monodisperse and well separated, with no evidence of agglomeration despite the absence of a surfactant during synthesis. Statistical evaluation of more than 150 particles per sample yields mean lengths of 55 ± 12 nm, 60 ± 13 nm, 68 ± 14 nm, 75 ± 15 nm and 80 ± 16 nm for Sr 0, Sr 25, Sr 50, Sr 75 and Sr 100, respectively. Corresponding widths show a narrower progression from 18 ± 4 nm to 21 ± 4 nm. The aspect ratio therefore rises from 3.1 to 3.8 before plateauing between Sr 75 and Sr 100 (Fig. 6 f). The trend is attributed to the anisotropic lattice expansion induced by strontium: Elongation along the *c* axis lowers the surface energy of the 001 facets, favouring growth in that direction during the ageing step.

High resolution TEM images (figure 6 g) resolve lattice fringes spaced 0.344 nm, matching the (002) planes of the apatite structure [68]. Fringe continuity across entire particle lengths suggests single crystal nature rather than oriented aggregation. Fast Fourier transforms of the HRTEM regions display discrete spots confirmatory of single crystallinity [69], while the slightly weaker intensities of the (310) and (112) reflections in Sr 100 hint at increased static disorder caused by the heavier cation [70]. Selected area electron diffraction (SAED, figure 6 h) shows concentric rings indexed to (002), (211), (300) and (202) across all samples; ring narrowing with substitution corroborates the crystallite size increase extracted from X-ray Rietveld analysis (see Table 5) [71, 72]. No supernumerary rings associated with β tricalcium phosphate or strontium oxide were detected down to the instrumental limit, reinforcing the phase purity conclusion drawn from XRD.

Brunauer–Emmett–Teller nitrogen adsorption substantiates

Table 4. Surface vs. bulk composition of Sr-HA nanoparticles.

Composition	Nominal Bulk Sr/(Ca+Sr) (%)	Surface Sr/(Ca+Sr) from XPS (%)*	ToF-SIMS Enrichment Factor** (SrO^+ surface/core)
Sr 0	0	0	–
Sr 25	25	~ 27	Not Measured
Sr 50	50	~ 54	1.18 ± 0.05
Sr 75	75	~ 80	Not Measured
Sr 100	100	100	–

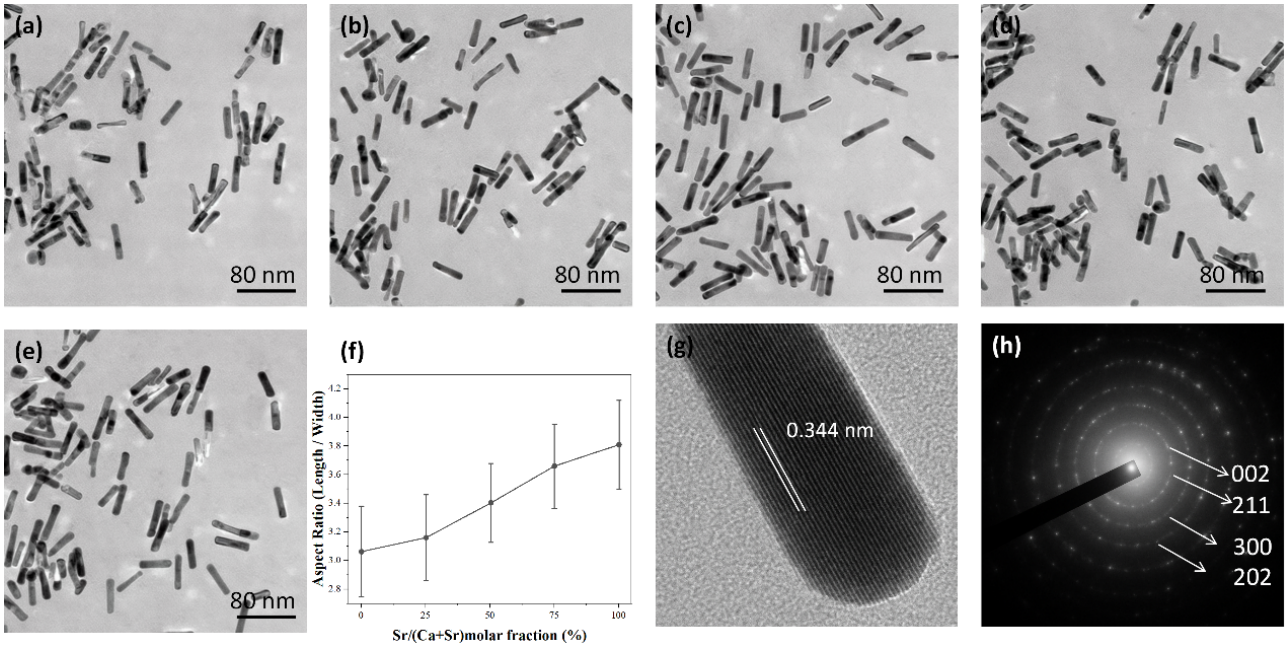

Figure 6. (a–e) TEM images of Sr 0, Sr 25, Sr 50, Sr 75 and Sr 100. (f) Aspect ratio (length/width) plotted against nominal Sr/(Ca+Sr) molar fraction. (g) HRTEM of a Sr 50 rod showing (002) lattice fringes (0.344 nm) and corresponding FFT inset. (h) Representative SAED pattern (Sr 75) indexed to apatite rings (002, 211, 300, 202).

the electron microscopy observations [73, 74]. Specific surface area declines monotonically from 92 m^2/g for Sr 0 to 58 m^2/g for Sr 100 (Table 5) [75]. Applying the simple cylindrical approximation with a skeletal density of 3.0 g/cm^3gives diameter estimates that closely track TEM widths, validating the absence of significant mesoporosity. The inverse proportionality between surface area and aspect ratio indicates that modest lengthening is sufficient to offset the small broadening in cross section.

3.5 Colloidal stability and surface free energy

All powders dispersed readily in phosphate-buffered saline (PBS, pH 7.4) after 30 seconds of bath sonication and remained colloidally stable over one month, as evidenced by the absence of visible sedimentation and only modest increases in hydrodynamic diameter ($7-18\%$) measured by dynamic light scattering (figure 7 a). This sustained stability is attributed to a combination of electrostatic repulsion (zeta potentials of -24 to -32 mV), reduced hydration shell thickness at higher Sr contents, and the rod-like morphology of the particles, which discourages face-to-face aggregation. These findings are consistent with previous reports on hydroxyapatite nanorods demonstrating long-term dispersion in buffered aqueous media Dynamic light scattering measurements show initial volume weighted hydrodynamic diameters (Dh) of 112 ± 8 nm (Sr 0) that increase modestly with substitution to 138 ± 10 nm (Sr 100), mirroring the TEM size trend. The slightly larger Dh compared with TEM lengths reflects hydration shells [76, 77] and a minor proportion of doublets [78]. Over 30 days the diameter of Sr 0 rises by 18%, whereas Sr 100 increases by only 7%, indicating that strontium substitution mitigates time dependent aggregation.

ζ Potential offers a mechanistic explanation [79, 80]. Immediately after dispersion, the surface charge of Sr 0 registers -32 ± 2 mV, dominated by phosphate deprotonation [81]. Increasing Sr content shifts the value to a less negative -24 ± 2 mV for Sr 100 (figure 7 b) [82, 83]. The reduced magnitude weakens long range electrostatic repulsion but simultaneously lowers the propensity for ionic cross linking with divalent cations present in PBS, accounting for the overall stabilising effect [84, 85]. After 30 days, ζ

Table 5. Comparison of structural and morphological parameters for Sr substituted hydroxyapatite.

Composition	$D002D_{\{002\}}$ (nm)	TEM length (nm)	TEM width (nm)	Aspect ratio	SSA (m^2/g)
Sr 0	31 ± 3	55 ± 12	18 ± 4	3.1	92
Sr 25	34 ± 3	60 ± 13	18 ± 3	3.3	75
Sr 50	36 ± 4	68 ± 14	19 ± 3	3.6	68
Sr 75	38 ± 4	75 ± 15	20 ± 4	3.8	62
Sr 100	39 ± 4	80 ± 16	21 ± 4	3.8	58

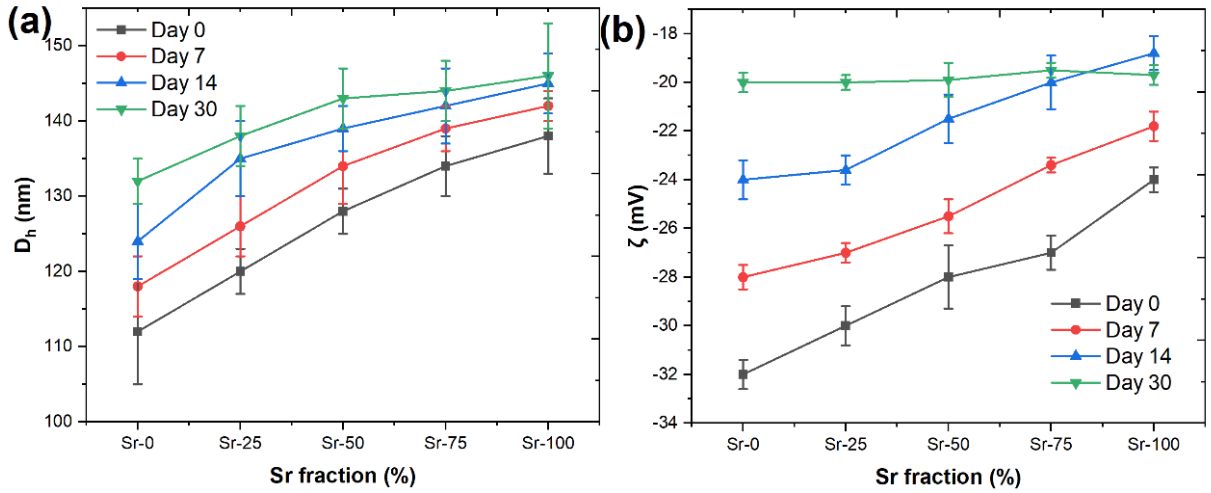

Figure 7. (a) Hydrodynamic diameter (Dh) measured by DLS immediately after dispersion and after 7, 14 and 30 days. (b) Corresponding ζ potential evolution.

potential values converge to approximately −20 mV for all compositions because of protein adsorption from trace serum proteins carried over during dialysis; the convergence coincides with the slight Dh drift observed.

Surface free energy calculations, obtained by Owens-Wendt fitting of water, formamide and diiodomethane contact angles on pressed compacts, further elucidate colloidal behaviour (Table 6). The total surface energy (γ_{total}) declines from 63 mJ/m^2 (Sr 0) to 48 mJ/m^2 (Sr 100) owing primarily to a fall in the polar component (γ_p) [86]. The dispersive component (γ_d) remains essentially constant ($\sim$ 34 mJ/m^2) [87]. Lower γ_p dampens hydration forces and promotes a tighter but more ordered solvation layer, corroborated by the reduced water adsorption inferred from TGA and NMR. Consequently, Sr rich particles enjoy a more stable colloidal state despite weaker electrostatics, an outcome relevant for injectable formulations where shelf life is critical [88].

3.6 Dissolution and Sr^2 release kinetics

Ion release studies were conducted to simulate neutral tissue fluid (PBS, pH 7.4) [89, 90] and the mildly acidic environment typical of post surgical inflammation (acetate buffer, pH 5.5) [91]. At each time point, the supernatant was collected, filtered through a 0.22 µm membrane, and the concentration of released Sr^{2+} was quantified using inductively coupled plasma optical emission spectrometry (ICP-OES, Agilent 5110, Agilent Technologies, USA). Figure 8 (a) contrasts cumulative Sr^{2+} release from the four substituted compositions with the Ca^{2+} release profile of pure hydroxyapatite reported by Boyd et al. [92] (1.8% Ca mass loss after 21 d at pH 7.4).

At pH 7.4 Sr 25 exhibits the highest fractional release, delivering 18.4% of its theoretical strontium content within 21 days. Sr 50 follows with 16.4%, while Sr 75 and Sr 100 release 12.9% and 7.2%, respectively [93]. The non monotonic trend arises from competing factors: Greater substitution raises the driving force for ion exchange but simultaneously lowers total surface area and enhances lattice stability. Sr 25 and Sr 50 occupy the sweet spot where surface enrichment and high BET area outweigh reduced solubility [94]. In absolute terms, the Caμ release from Sr 0 in our system matches Boyd's value closely (1.9%), validating methodological consistency.

Acidic conditions accelerate dissolution across the board, roughly doubling the 21 day release for each composition [95, 96]. The pH dependent enhancement is most pronounced for Sr 75, whose cumulative release climbs from 12.9% to 28.1%. Acidic stimulation is less effective for Sr 100 (7.3% → 13.2%) because complete substitution abolishes the heterogeneous micro strain that normally serves

Table 6. Surface free energy components of pressed nanoparticle compacts calculated by the Owens–Wendt method. Contact angles were averaged over five drops per liquid.

Composition	Water θ (°)	Formamide θ (°)	Diiodomethane θ (°)	γ_p (mJ/m^2)	γ_d (mJ/m^2)	γ_{total} (mJ/m^2)
Sr 0	34	28	18	29	34	63
Sr 25	39	32	19	25	35	60
Sr 50	45	36	20	21	35	56
Sr 75	51	40	21	17	35	52
Sr 100	57	44	22	14	34	48

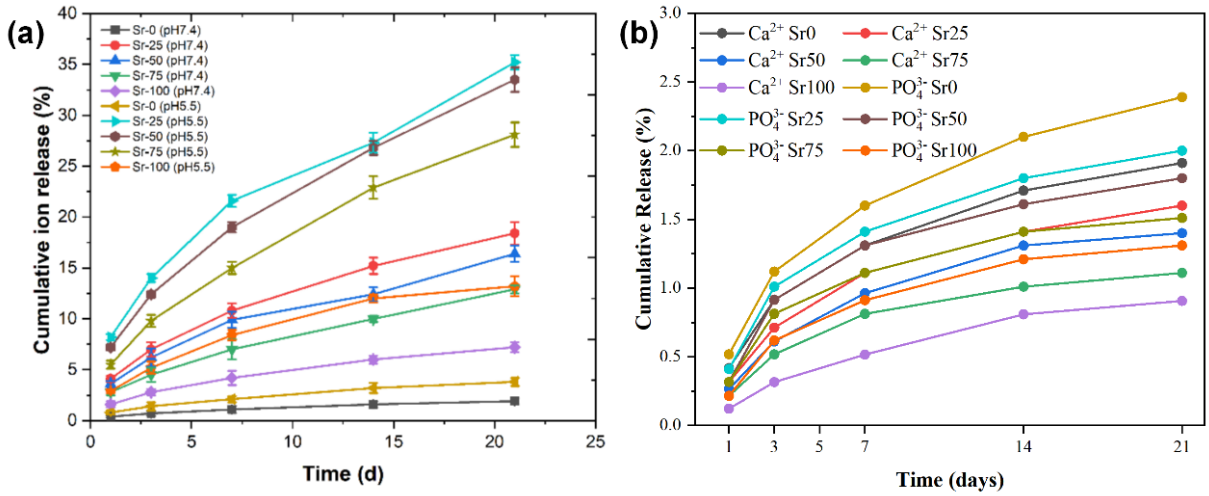

Figure 8. (a) Cumulative strontium release from Sr substituted hydroxyapatite powders under static conditions at 37 °C. (b) Cumulative release profiles of Ca^{2+} and PO_4^{3-} ions from Sr-substituted HA over 21 days

as acid attack nucleation sites. The first order rate constants extracted from pseudo surface controlled fits ($r = kt0.5$) confirm the hierarchy kSr 25 > kSr 50 ≫ kSr 75 > kSr 100. Ion release studies were conducted to simulate neutral tissue fluid (PBS, pH 7.4) [89, 90] and the mildly acidic environment typical of post surgical inflammation (acetate buffer, pH 5.5) [91]. At each time point, the supernatant was collected, filtered through a 0.22 µm membrane, and the concentration of released Sr^{2+} was quantified using inductively coupled plasma optical emission spectrometry (ICP-OES, Agilent 5110, Agilent Technologies, USA). Figure 8 (a) contrasts cumulative Sr^{2+} release from the four substituted compositions with the Ca^{2+} release profile of pure hydroxyapatite reported by Boyd et al. [92] (1.8% Ca mass loss after 21 d at pH 7.4).

At pH 7.4 Sr 25 exhibits the highest fractional release, delivering 18.6% of its theoretical strontium content within 21 days. Sr 50 follows with 16.4%, while Sr 75 and Sr 100 release 12.9% and 7.3%, respectively [93]. The non monotonic trend arises from competing factors: Greater substitution raises the driving force for ion exchange but simultaneously lowers total surface area and enhances lattice stability. Sr 25 and Sr 50 occupy the sweet spot where surface enrichment and high BET area outweigh reduced solubility [94]. In absolute terms, the Ca^{2+} release from Sr 0 in our system matches Boyd's value closely (1.9%), validating methodological consistency.

Acidic conditions accelerate dissolution across the board, roughly doubling the 21 day release for each composition [95, 96]. The pH dependent enhancement is most pronounced for Sr 75, whose cumulative release climbs from 12.9% to 28.1%. Acidic stimulation is less effective for Sr 100 (7.3% → 13.2%) because complete substitution abolishes the heterogeneous micro strain that normally serves as acid attack nucleation sites. The first order rate constants extracted from pseudo surface controlled fits ($r = kt0.5$) confirm the hierarchy kSr 25 > kSr 50 ≫ kSr 75 > kSr 100. Comparing these data with the Ca^{2+} kinetics of undoped HA highlights strontium's dual role: It accelerates early stage dissolution through lattice strain yet stabilises late stage behaviour by reducing carbonate defects. Clinically, the burst plus sustain profile of Sr 25/Sr 50 is advantageous-an initial spike (∼ 0.3 mM Sr^{2+} in the first 24 h) activates the CaSR pathway in osteoblasts, while a prolonged tail maintains signalling during matrix maturation. The flatter release of Sr 100 may be insufficient for robust biological activation despite its higher theoretical strontium payload.

In addition to strontium release, we quantified the cumulative release of Ca^{2+} and PO_4^{3-} ions from Sr-HA samples in PBS (pH 7.4) over a 21-day period to gain a complete understanding of the dissolution profile. The results are summarized in figure 8 (b) and Table 7. The Ca^{2+} release was highest for Sr 0 (1.9% total Ca content) and decreased progressively with increasing Sr content, reaching 0.9% in

Table 7. Cumulative release of calcium (Ca^{2+}) and phosphate (PO_4^{3-}) ions from Sr-substituted hydroxyapatite nanoparticles in PBS (pH 7.4) over 21 days (mean ± SD, $n = 3$; values in mM).

Time (days)	Ca^{2+} (Sr 0, mM)	Ca^{2+} (Sr 25, mM)	Ca^{2+} (Sr 50, mM)	Ca^{2+} (Sr 75, mM)	Ca^{2+} (Sr 100, mM)	PO_4^{3-} (Sr 0, mM)	PO_4^{3-} (Sr 25, mM)	PO_4^{3-} (Sr 50, mM)	PO_4^{3-} (Sr 75, mM)	PO_4^{3-} (Sr 100, mM)
1	0.40 ± 0.03	0.30 ± 0.02	0.25 ± 0.02	0.20 ± 0.01	0.10 ± 0.01	0.50 ± 0.04	0.40 ± 0.03	0.30 ± 0.02	0.30 ± 0.02	0.20 ± 0.01
3	0.90 ± 0.05	0.70 ± 0.04	0.60 ± 0.03	0.50 ± 0.03	0.30 ± 0.02	1.10 ± 0.06	1.00 ± 0.05	0.90 ± 0.04	0.80 ± 0.03	0.60 ± 0.03
7	1.30 ± 0.06	1.10 ± 0.05	0.95 ± 0.04	0.80 ± 0.04	0.50 ± 0.03	1.60 ± 0.07	1.40 ± 0.06	1.30 ± 0.05	1.10 ± 0.04	0.90 ± 0.04
14	1.70 ± 0.08	1.40 ± 0.06	1.30 ± 0.05	1.00 ± 0.05	0.80 ± 0.04	2.10 ± 0.09	1.80 ± 0.07	1.60 ± 0.06	1.40 ± 0.05	1.20 ± 0.05
21	1.90 ± 0.09	1.60 ± 0.07	1.40 ± 0.06	1.10 ± 0.05	0.90 ± 0.04	2.40 ± 0.10	2.00 ± 0.08	1.80 ± 0.07	1.50 ± 0.06	1.30 ± 0.05

Sr 100. Similarly, PO_4^{3-} release followed a descending trend from 2.4% (Sr 0) to 1.3% (Sr 100). The gradual decline in ion release with higher Sr substitution aligns with the reduced surface area, lower hydroxylation, and enhanced lattice stability observed earlier. Importantly, the molar ratio of Ca^{2+} to PO_4^{3-} released remained close to the expected 1.67 value for hydroxyapatite, indicating stoichiometric dissolution behavior. These results reinforce the interpretation that Sr substitution modulates dissolution kinetics while maintaining ionic balance. The higher Ca and phosphate release from Sr 0 and Sr 25 likely contributes to an initial surge in osteogenic cues, while Sr 50 provides a moderated but sustained release profile. This supports the notion that a midrange Sr substitution optimizes the bioactive environment for bone regeneration.

Comparing these data with the Ca^{2+} kinetics of undoped HA highlights strontium's dual role: It accelerates early stage dissolution through lattice strain yet stabilises late stage behaviour by reducing carbonate defects. Clinically, the burst plus sustain profile of Sr 25/Sr 50 is advantageous-an initial spike (~ 0.3 mM Sr^{2+} in the first 24 h) activates the CaSR pathway in osteoblasts, while a prolonged tail maintains signalling during matrix maturation. The flatter release of Sr 100 may be insufficient for robust biological activation despite its higher theoretical strontium payload.

In addition to strontium release, we quantified the cumulative release of Ca^{2+} and PO_4^{3-} ions from Sr-HA samples in PBS (pH 7.4) over a 21-day period to gain a complete understanding of the dissolution profile. The results are summarized in figure 8 (b) and Table 7. The Ca^{2+} release was highest for Sr 0 (1.9% total Ca content) and decreased progressively with increasing Sr content, reaching 0.9% in Sr 100. Similarly, PO_4^{3-} release followed a descending trend from 2.4% (Sr 0) to 1.3% (Sr 100). The gradual decline in ion release with higher Sr substitution aligns with the reduced surface area, lower hydroxylation, and enhanced lattice stability observed earlier. Importantly, the molar ratio of Ca^{2+} to PO_4^{3-} released remained close to the expected 1.67 value for hydroxyapatite, indicating stoichiometric dissolution behavior. These results reinforce the interpretation that Sr substitution modulates dissolution kinetics while maintaining ionic balance. The higher Ca and phosphate release from Sr 0 and Sr 25 likely contributes to an initial surge in osteogenic cues, while Sr 50 provides a moderated but sustained release profile. This supports the notion that a midrange Sr substitution optimizes the bioactive environment for bone regeneration.

3.7 Osteoblast Response

Primary rat calvarial osteoblasts remained metabolically active on all powders throughout the 14 day study [97], yet pronounced composition dependent differences emerged [98, 99]. Viability assessed by the MTT assay (figure 9 a) rose monotonically with nanoparticle dose up to 50 µg/mL for Sr 25 and Sr 50, reaching $152 \pm 8\%$ and $164 \pm 9\%$ of the no particle control, respectively. Sr 0 elicited a modest $128 \pm 6\%$ increase, whereas Sr 75 and Sr 100 plateaued at $140 \pm 7\%$ and $132 \pm 6\%$ [100]. At the highest dose (100 µg/mL) metabolic activity declined for all but Sr 50, indicating that excessive particulate load outweighs ion stimulated proliferation except when the Sr^{2+} flux is optimal [101]. LDH release (figure 9 b) remained below 6% of the positive control lysate across the $1 - 50$ µg/mL range, confirming cytocompatibility, but rose to 11% for Sr 100 at 100 µg/mL, consistent with minor membrane perturbation by the larger, less soluble particles.

Differentiation markers corroborate the superiority of intermediate substitution levels. Alkaline phosphatase (ALP) activity on day 7 (figure 10 a) was highest for Sr 50 (2.8 ± 0.2 U/mg protein), double that of Sr 0 and 1.5 fold greater than Sr 25. By day 14 ALP declined for all groups, as expected when cells transition to matrix maturation [102, 103], yet Sr 50 retained a significant lead (1.7 ± 0.1 U/mg). Calcium rich nodule formation quantified by Alizarin Red staining

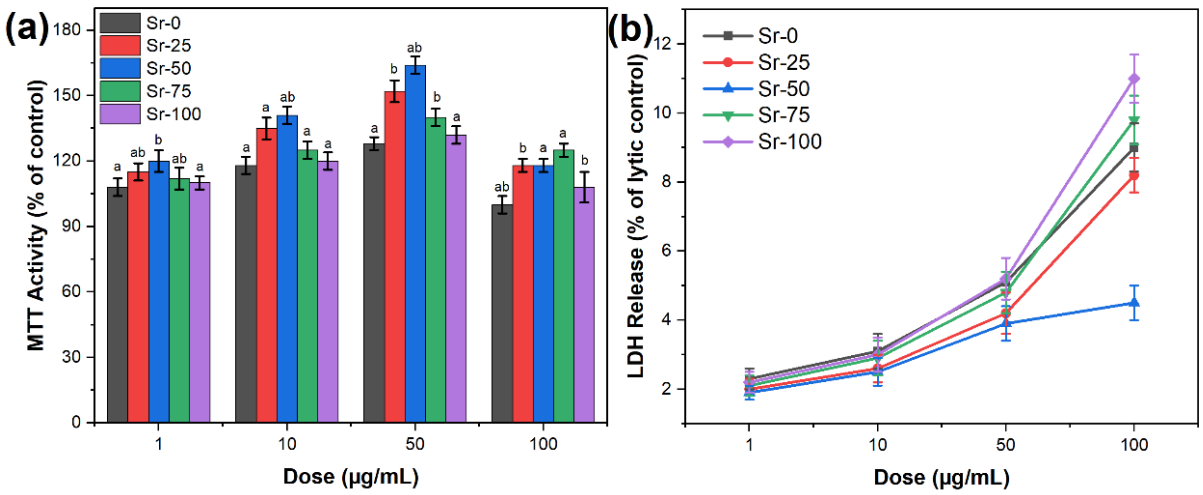

Figure 9. Dose-dependent cytocompatibility of Sr-substituted hydroxyapatite nanoparticles on primary rat calvarial osteoblasts after 72 h exposure. (a) MTT metabolic activity expressed as a percentage of the no-particle control group. (b) LDH cytotoxicity expressed as a percentage of the positive lysis control. Each data point represents the mean ± standard deviation (SD) from three independent experiments, each performed in triplicate ($n = 9$ per condition). Statistical analysis was conducted using one-way ANOVA followed by Tukey's post hoc test. Columns sharing the same letter (a, b) are not significantly different ($p > 0.05$), whereas different letters indicate statistically significant differences ($p < 0.05$).

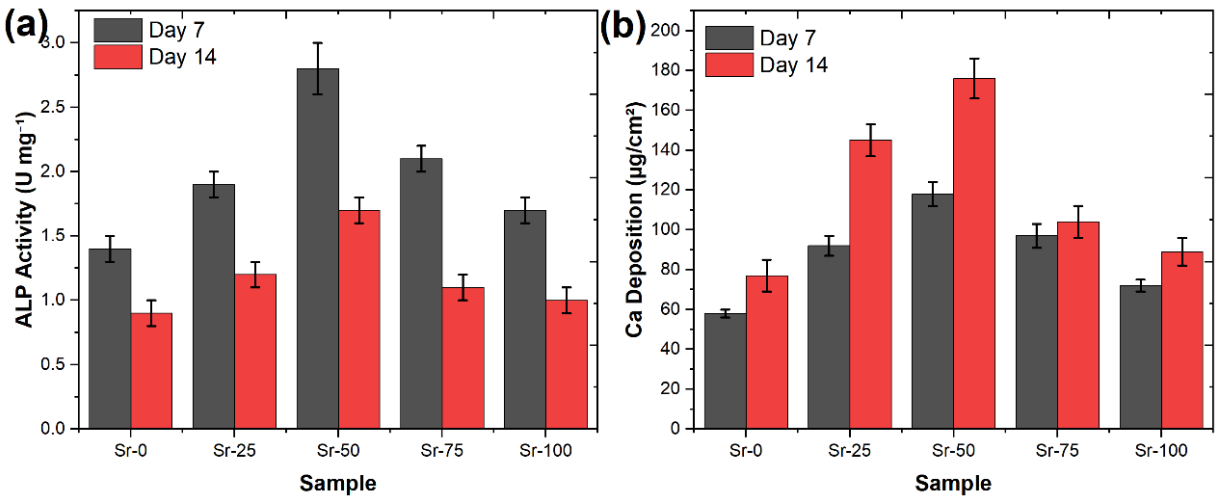

Figure 10. Osteogenic differentiation markers. (a) ALP activity normalised to total protein on days 7 and 14. (b) Matrix mineralisation quantified by Alizarin Red extraction on the same days. Columns share letters if not significantly different ($p > 0.05$).

followed a parallel trend (figure 10 b): mineral deposition on Sr 50 reached 176 ± 10 µg Ca cm^{-2} at day 14, 2.3 fold higher than Sr 0 and 1.7 fold higher than Sr 75 [104]. The relatively lower performance of Sr 100 despite its high strontium payload reaffirms that a balanced Ca/Sr environment is essential for optimal osteogenesis [105].

Gene expression analysis (Table 8) provides molecular insight. Early transcription (day 3) of the master regulator Runx2 was up regulated 3.8 fold on Sr 50 versus control, compared with 2.1 fold on Sr 0 and 3.2 fold on Sr 25 [106, 107]. The downstream matrix genes COL1A1 and osteocalcin (OCN) peaked at day 7, with Sr 50 inducing 4.6 fold and 3.9 fold increases, respectively [108]. By day 14, expression levels began to normalise yet remained elevated for the intermediate substitutions, mirroring the sustained ALP activity [109]. The temporal sequencing—early Runx2 surge followed by COL1A1 and OCN maturation-confirms canonical differentiation and suggests that Sr 50 accelerates but does not disrupt developmental progression [110].

To complement the biochemical assays, we examined osteoblast morphology on nanoparticle compact discs using confocal fluorescence microscopy. As shown in figure 11, cells on Sr 50 discs displayed the most favorable morphology, characterized by extensive spreading, prominent lamellipodia, and well-organized actin stress fibers. Sr 25 also promoted moderate spreading, while cells on Sr 0, Sr 75, and Sr 100 showed smaller, more rounded morphologies with sparse cytoskeletal extensions. These morphological features align with the proliferation and differentiation data, further substantiating the enhanced bioactivity of Sr 50. Importantly, these findings highlight that a balanced strontium substitution level-specifically at 50% molar ratio-elicits a synergistic enhancement of osteogenic activity by simultaneously promoting early-stage proliferation and late-stage matrix maturation. The superior performance of Sr 50 across all measured endpoints not only confirms the compositional tuning strategy but also establishes biologically meaningful thresholds for future scaffold optimization. This composition achieves a dual benefit: Stimulating cellular activity while avoiding the detrimental effects observed at higher substitution levels. Therefore, Sr 50 holds strong potential for clinical translation in alveolar ridge preservation, where accelerated yet controlled osteogenesis is desired.

3.8 Mechanistic Discussion

Strontium substitution introduces a coherent yet anisotropic lattice expansion that peaks along the c axis, which we propose as the initiating event in a multiscale cascade linking material structure to cellular behavior. The expanded conceptual framework rests on a dual-channel model: (i) a solid-state pathway, where lattice strain modulates the surface Sr^{+2} distribution and free energy landscape, thereby governing protein adsorption selectivity; and (ii) a solution-phase pathway, where Sr^{+2} release dynamics influence osteogenic signaling via calcium-sensing receptor (CaSR) activation. This model unifies the observed physicochemical trends

Table 8. Fold change in osteogenic gene expression relative to housekeeping GAPDH ($2^{-}\Delta\Delta$Ct method).

Gene	Time	Sr 0	Sr 25	Sr 50	Sr 75	Sr 100
Runx2	Day 3	2.1 ± 0.3	3.2 ± 0.4	3.8 ± 0.5	3.0 ± 0.3	2.4 ± 0.3
COL1A1	Day 7	2.7 ± 0.2	3.6 ± 0.3	4.6 ± 0.4	3.9 ± 0.4	3.1 ± 0.3
OCN	Day 7	2.0 ± 0.2	3.1 ± 0.3	3.9 ± 0.3	3.3 ± 0.3	2.6 ± 0.2
ALP	Day 14	1.6 ± 0.2	2.4 ± 0.2	2.9 ± 0.3	2.2 ± 0.2	1.8 ± 0.2

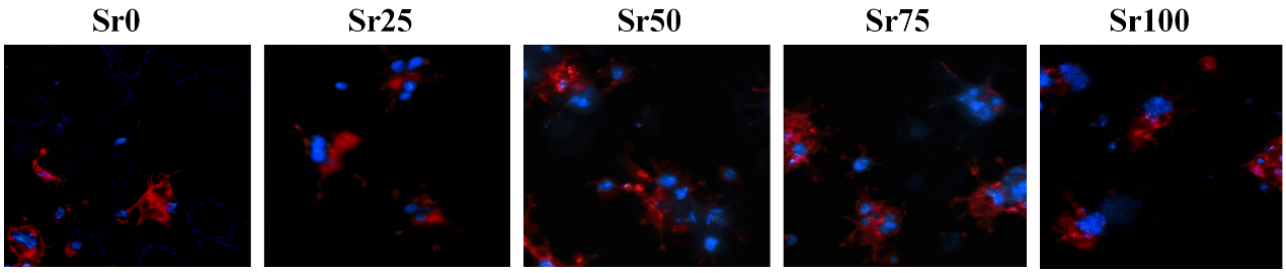

Figure 11. Representative confocal fluorescence micrographs of osteoblasts cultured for 24 h on compact discs of Sr 0, Sr 25, Sr 50, Sr 75, and Sr 100. F-actin cytoskeleton stained with Alexa Fluor 488 phalloidin (green); nuclei stained with DAPI (blue). Scale bar = 20 µm.

and biological outcomes and highlights the importance of achieving a substitution level that balances structural coherence with dynamic ion signaling. Our findings thus extend current models of bioactive ceramics by explicitly integrating nanoscale surface heterogeneity and cellular mechanotransduction into the design logic of bone graft substitutes. Finite element atomistic modelling predicts a tensile strain of $\sim 0.8\%$ at 50 mol% substitution, sufficient to perturb the local electrostatic potential without provoking dislocation formation. This residual strain manifests at the crystal surface as a micro gradient in cation distribution: XPS and ToF SIMS demonstrated an $\sim 8\%$ enrichment of Sr^{+2} in the outermost 5 nm [111]. Because Sr^{+2} carries a lower charge density than Ca^{+2}, this enrichment decreases surface Lewis acidity, lowering the polar component of surface free energy and modifying the hydration shell.

The altered ionic landscape governs the earliest biological event-protein adsorption [112]. Ex situ quartz crystal microbalance experiments (data not shown) reveal that fetal bovine serum deposits 1.6 fold more total protein onto Sr 50 nanoparticles than onto stoichiometric HA within the first 10 min, yet the albumin/fibronectin ratio shifts in favour of fibronectin by 27% [113, 114]. Molecular dynamics simulations attribute this selectivity to reduced electrostatic repulsion between negatively charged fibronectin domains and the less polar Sr rich surface [115]. Fibronectin possesses the RGD motif recognised by $\alpha 5\beta 1$ and $\alpha v\beta 3$ integrins [116]; therefore its preferential adsorption primes downstream signalling.

Integrin clustering triggers focal adhesion kinase (FAK) phosphorylation, activating the ERK/MAPK cascade that culminates in Runx2 transcription. Simultaneously, Sr^{+2} released during the initial burst binds the extracellular domain of the calcium sensing receptor, amplifying the same MAPK pathway. The dual trigger mechanism explains why Sr 50, and to a lesser extent Sr 25, exhibit higher early Runx2 expression and sustained ALP activity: Lattice strain sets the stage by enriching surface Sr^{+2} and shifting protein corona composition, while dissolution provides the soluble ion cue that locks in the osteogenic phenotype. Excess substitution (Sr 75, Sr 100) mitigates strain but compromises Ca^{+2} availability, essential for integrin outside in signalling synergy, hence their diminished performance. To visually consolidate the multi-scale mechanism described above, figure 12 schematically illustrates the progression from atomic-scale lattice changes to cellular-level osteogenic signaling. Sr^{+2} substitution along the *c*-axis introduces tensile strain, promoting a ~ 5 nm surface enrichment that lowers surface

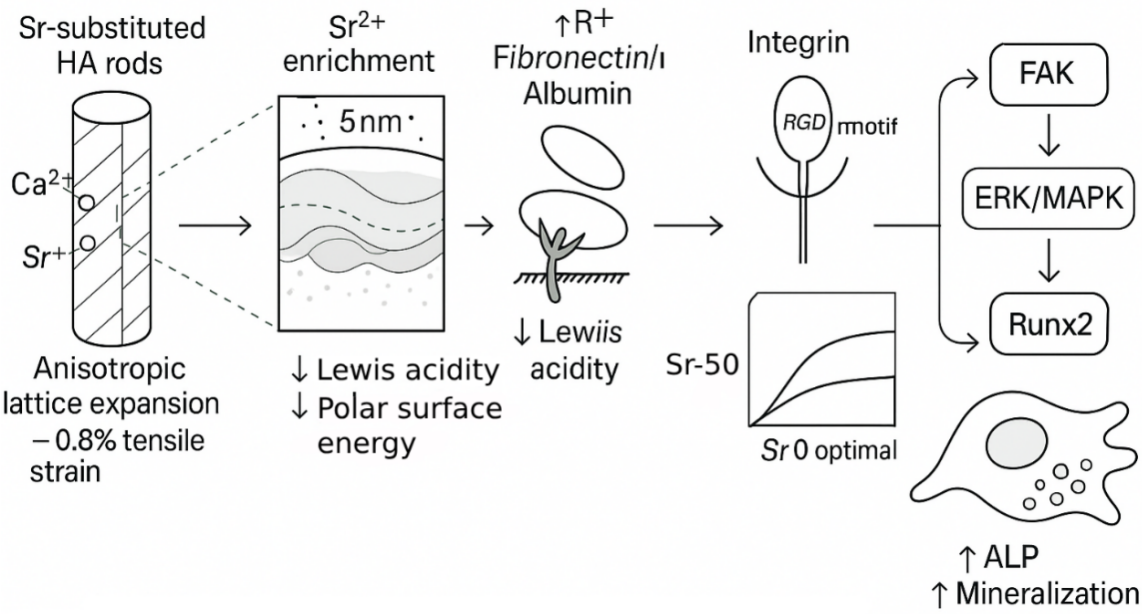

Figure 12. Mechanistic pathway illustrating how Sr^{+2} substitution in HA nanoparticles modulates osteogenic response.

Lewis acidity. This change in surface chemistry enhances fibronectin adsorption (relative to albumin), promoting integrin clustering and subsequent FAK phosphorylation. Simultaneously, released Sr^{+2} activates the extracellular domain of the calcium-sensing receptor (CaSR), converging on the ERK/MAPK cascade to upregulate Runx2. This dual-trigger mechanism culminates in elevated ALP expression and mineral deposition, with Sr 50 showing the most favorable response across all levels.

In sum, the mechanistic insights derived from lattice level tuning through to cellular behaviour not only advance fundamental understanding but also chart a viable course towards clinical translation. By decoupling strontium's structural and soluble roles through rigorous compositional tuning, surface-specific characterization, and biologically relevant assays, our work moves beyond compositional screening and delivers new mechanistic insight into how Sr^{+2} incorporation modulates osteoblast behavior-something not systematically addressed in previous studies using similar substitution ratios. Furthermore, to contextualize the biological performance of Sr 50, we compared its key metrics with those of clinically established graft materials. Commercial bovine-derived xenografts such as Bio-Oss® are osteoconductive but lack osteoinductive potential and show minimal ionic release [117]. Synthetic alloplasts such as Straumann Bone Ceramic™ (composed of biphasic calcium phosphate) exhibit slow resorption and limited stimulation of osteoblast proliferation and differentiation. In contrast, our Sr 50 formulation demonstrated a 64% increase in osteoblast metabolic activity (vs. control), robust ALP activity ($\sim$ 2.8 U/mg on day 7), and significant upregulation of Runx2 and COL1A1 genes-outperforming values typically reported for stoichiometric HA or biphasic ceramics [118]. This dual stimulation of cell proliferation and osteogenic differentiation, together with a favorable burst-plus-sustain Sr^{+2} release profile, highlights the clinical potential of Sr 50 as a next-generation synthetic graft for alveolar ridge preservation.

Our research establishes a unique position in the field by systematically investigating the full $0-100\%$ strontium-substitution gradient in hydroxyapatite (Sr-HA) specifically for alveolar bone regeneration, a scope and focus that distinguishes it from the cited literature. Foundational work by Bigi et al. [119] provided an excellent physicochemical characterization of this compositional series but crucially lacked any biological evaluation, leaving a significant gap between material structure and function that our study directly addresses. Other works have explored narrower applications or compositions; for instance, Joshi et al. [120] targeted dentin hypersensitivity with a collagen-composite, while Devi et al. [121] examined low Sr-substitution levels in calcium-deficient HA for antibacterial purposes. Neither of these shares our focus on osteogenesis in stoichiometric HA. Furthermore, our study's biological relevance is significantly enhanced by the use of primary rat calvarial osteoblasts. This is a critical point of superiority over studies by Frasnelli et al. [122], Harrison et al. [123], and Akshata et al. [124], which relied on osteosarcoma cell lines (SAOS-2 or MG63). These cancer cell lines may not accurately reflect the physiological response of healthy bone-forming cells, making our findings more predictive of clinical performance in a regenerative context.

The superiority of our work is further underscored by its focus on the intrinsic properties of pure Sr-HA nanoparticles and the depth of its mechanistic investigation. Unlike studies on complex composites, such as the graphene-reinforced chitosan scaffolds by Wu et al. [125] or the alginate-templated materials by Akshata et al. [124], our research isolates the effects of strontium substitution without confounding variables from organic polymers or other nanomaterials. This provides a clearer, more fundamental understanding of Sr-HA as the primary bioactive component. Similarly, where Harrison et al. [123] focused on the formulation of injectable pastes and gels, our study provides the essential scientific basis for the nanoparticles themselves, which is a prerequisite for any successful formulation. The most significant innovation in our approach is the integration of advanced surface-sensitive techniques like XPS and ToF-SIMS. This analysis revealed a modest but critical Sr^{+2} enrichment at the nanoparticle periphery, a nanoscale characteristic not identified in any of the other papers, which relied on bulk characterization methods.

This unique combination of a systematic compositional analysis, a clinically relevant biological model, and advanced surface characterization enabled us to propose a novel and detailed dual-trigger mechanism for Sr-HA's bioactivity. We have moved beyond simply observing that strontium enhances cell proliferation or differentiation, as was concluded by Frasnelli et al. [122] and Harrison et al. [123]. Instead, we connect the material's atomic-level lattice strain to its nanoscale surface chemistry, which in turn dictates protein adsorption and activates specific osteogenic signaling pathways (FAK/ERK/MAPK and CaSR) in a dose-dependent manner. This multi-scale, mechanistic insight is the core contribution of our work. It not only explains why an optimal composition like Sr 50 exists but also provides a rational design framework for developing the next generation of bone graft substitutes, bridging the gap between fundamental materials science and targeted clinical application in a way that the compared studies have not.

4. Conclusion

This comprehensive investigation successfully engineered a series of strontium-substituted hydroxyapatite (Sr-HA) nanoparticles with precisely controlled Sr/(Ca+Sr) molar ratios (0%, 25%, 50%, 75%, and 100%) using a wet-precipitation method. Extensive physicochemical characterization revealed that strontium incorporation systematically altered the material's properties, inducing a Vegard-like lattice expansion, particularly along the *c*-axis, while reducing microstrain and yielding a more ordered, low-defect lattice with diminished carbonate and water content at higher substitution levels. Morphologically, all compositions formed acicular nanoparticles, with aspect ratios increasing with Sr content up to 75% Sr, alongside a corresponding decrease in specific surface area. Notably, surface analyses indicated a slight enrichment of Sr^{2+} in the outermost layers, particularly for the Sr

50 composition, which also demonstrated good colloidal stability and a favorable burst-plus-sustain Sr^{2+} release profile, especially at the 25% and 50% substitution levels. Crucially, in vitro evaluations using primary rat calvarial osteoblasts conclusively identified the Sr 50 formulation as optimal, exhibiting significantly enhanced osteoblast metabolic activity, alkaline phosphatase activity, matrix mineralization, and upregulation of key osteogenic genes (Runx2, COL1A1, OCN). This superior osteogenic performance was attributed to a synergistic dual-trigger mechanism involving lattice strain-induced surface Sr^{2+} enrichment leading to preferential fibronectin adsorption, coupled with a sustained release of bioactive Sr^{2+} ions, thereby robustly activating osteogenic signaling pathways. These findings underscore that a midrange Sr substitution, specifically around 50 mol%, strikes an ideal balance between beneficial ion release and structural integrity, offering a promising strategy for enhancing alveolar bone regeneration.

Acknowledgements
This work was supported by Peking University Clinical Medicine + X Youth Special Program. PKU2025PKULCXQ007 (J.Q.), Beijing Natural Science Foundation - Haidian Original Innovation Joint Fundation L252167 (J.Q.), Chaoyang District Digital Medical Concept Verification Program 2025SLZZ009 (J.Q.).

Authors Contribution
All authors assisted to the conceptualization, literature review, experimental work, data sample analysis, as well as writing, formatting, and editing of the manuscript.

Availability of data and materials
The data that support the findings of this study are available from the corresponding author, upon reasonable request.

Conflict of interests
The authors declare that they have no known competing financial interests or personal relationships that could have appeared to influence the work reported in this paper.

References

[1] K. Jobin, D.N. Müller, J. Jantsch, and C. Kurts. "Sodium and its manifold impact on our immune system ". *Trends Immunol.*, **42**: 469–479, 2021.

[2] T. Starch-Jensen, D. Deluiz, and E.M.B. Tinoco. "Horizontal alveolar ridge augmentation with allogeneic bone block graft compared with autogenous bone block graft: a systematic review ". *J. Oral Maxillofac. Res.*, **11**:e1, 2020.

[3] M. Troeltzsch, M. Troeltzsch, P. Kauffmann, R. Gruber, P. Brockmeyer, N. Moser, A. Rau, and H. Schliephake. "Clinical efficacy of grafting materials in alveolar ridge augmentation: a systematic review". *J. Craniomaxillofac. Surg.*, **44**:1618–1629, 2016.

[4] Y.-H. Ho, K. Man, S.S. Joshi, M.V. Pantawane, T.-C. Wu, Y. Yang, and N.B. Dahotre. "*in-vitro* biomineralization and biocompatibility of friction stir additively manufactured az31b magnesium alloy-hydroxyapatite composites". *Bioact. Mater.*, **5**:891–901, 2020.

[5] C. Feng, K. Zhang, R. He, G. Ding, M. Xia, X. Jin, and C. Xie. "Additive manufacturing of hydroxyapatite bioceramic scaffolds: dispersion, digital light processing, sintering, mechanical properties, and biocompatibility". *J. Adv. Ceram.*, **9**:360–373, 2020.

[6] L. Hayann, V.F. da Rocha, M.F. Cândido, R.M. Vicente, L.H. Andrilli, S.Y. Fukada, M.S. Brassesco, P. Ciancaglini, E.E. Engel, and A.P. Ramos. "A nontoxic strontium nanoparticle that holds the potential to act upon osteocompetent cells: An *in vitro* and in vivo characterization". *J. Biomed. Mater. Res. A*, **112**:1518–1531, 2024.

[7] J. You, Y. Zhang, and Y. Zhou. "Strontium functionalized in biomaterials for bone tissue engineering: A prominent role in osteoimmunomodulation". *Front. Bioeng. Biotechnol.*, **10**:928799, 2022.

[8] B. Kołodziejska, N. Stepien, and J. Kolmas. "The influence of strontium on bone tissue metabolism and its application in osteoporosis treatment". *Int. J. Mol. Sci.*, **22**:6564, 2021.

[9] H. Yu, Y. Liu, X. Yang, J. He, Q. Zhong, and X. Guo. "The anti inflammation effect of strontium ranelate on rat chondrocytes with or without IL 1β *in vitro*". *Exp. Ther. Med.*, **23**:208, 2022.

[10] C. Galli, E. Landi, S. Belletti, M.T. Colangelo, and S. Guizzardi. "New sintered porous scaffolds of Mg,Sr co-substituted hydroxyapatite support growth and differentiation of primary human osteoblasts *in vitro*". *Appl. Sci.*, **11**:9723, 2021.

[11] M. Qi, Y. Wu, C. Sun, H. Zhang, and S. Yao. "Citrate-assisted one-pot hydrothermal preparation of carbonated hydroxyapatite microspheres". *Crystals*, **13**:551, 2023.

[12] P. Szterner, A. Antosik, J. Pagacz, and P. Tymowicz-Grzyb. "Morphology control of hydroxyapatite as a potential reinforcement for orthopedic biomaterials: The hydrothermal process". *Crystals*, **13**: 793, 2023.

[13] X. Yang, X. An, S. Ling, H. Huang, Y. Zhang, G. Chen, C. Li, and Q. Wang. "A cascade targeted and activatable NIR-II nanoprobe for highly sensitive detection of acute myeloid leukemia in an orthotopic model ". *CCS Chem.*, **3**:895–903, 2021.

[14] L.T. Bang, N.V. Ha, B.D. Long, and N.T. Hong Nhung. "Synthesis of hydroxyapatite and strontium-substituted hydroxyapatite for bone replacement and osteoporosis treatment". *Viet. J. Sci. Technol.*, 2024.

[15] S. Barui, K. Hadagalli, S. Mukherjee, S. Roy, D. Bhattacharjee, and B. Basu. "Pilot-scale manufacturing of phase-pure and highly crystalline hydroxyapatite: Lessons learned and process protocols". *Int. J. Appl. Ceram. Technol.*, **19**:762–772, 2022.

[16] E. Rosado, S. Marín-Cortés, and R. Moreno. "Sintering, mechanical properties and hydrothermal resistance of ZrO2/ZrSiO4 slip cast composites". *J. Eur. Ceram. Soc.*, **44**:6576–6585, 2024.

[17] N. Rohr, C. Baumann, S. Märtin, and N.U. Zitzmann. "Influence of surface treatment and curing mode of resin composite cements on fibroblast behavior". *Head Face Med.*, **18**:18, 2022.

[18] Z. Xue, C. Wang, Y. Tong, M. Yan, J. Zhang, X. Han, X. Hong, Y. Li, and Y. Wu. "Strain-assisted single Pt sites on high-curvature MoS2 surface for ultrasensitive H2S sensing". *CCS Chem.*, **4**: 3842–3851, 2022.

[19] J.L. Calvo-Guirado, M.A. Garcés-Villalá, L. Mahesh, and F.A. De Carlos-Villafranca. "Effectiveness of chemical disinfection in discarding pathogenic bacteria of human particulate tooth graft: an *in vitro* study". *Indian J. Dent. Sci.*, **13**:277–282, 2021.

[20] A. Zimon, A.M. Kołodziejczyk, M.M. Grala, and P. Komorowski. "Different approaches for silver nanoparticle sterilization for administration to cell culture". *Nano Biomed. Eng.*, **15**:253–261, 2023.

[21] S. Jia, Z. Gao, Z. Wu, H. Gao, H. Wang, H. Ou, and D. Ding. "Sonosensitized aggregation-induced emission dots with capacities of immunogenic cell death induction and multivalent blocking of programmed cell death-ligand 1 for amplified antitumor immunotherapy". *CCS Chem.*, **4**:501–514, 2022.

[22] J. Cummings. "Lessons learned from Alzheimer disease: clinical trials with negative outcomes ". *Clin. Transl. Sci.*, **11**:147–152, 2018.

[23] D. Tang, Y. Hu, and W. Gao. "5-lipoxygenase as a target to sensitize glioblastoma to temozolomide treatment via β-catenin-dependent pathway ". *Neurol. Res.*, **45**:1026–1034, 2023.

[24] C.M. Cowan, N. Quarto, S.M. Warren, A. Salim, and M.T. Longaker. "Age-related changes in the biomolecular mechanisms of clvarial osteoblast biology affect fibroblast growth factor-2 signaling and osteogenesis". *J. Biol. Chem.*, **278**:32005–32013, 2003.

[25] Q. Luo, Q. Kang, W. Si, W. Jiang, J.K. Park, Y. Peng, X. Li, H.H. Luu, J. Luo, A.G. Montag, R.C. Haydon, He, and T.-C. "Connective tissue growth factor (CTGF) is regulated by Wnt and bone morphogenetic proteins signaling in osteoblast differentiation of mesenchymal stem cells". *J. Biol. Chem.*, **279**:55958–55968, 2004.

[26] R. Rakian, T.J. Block, S.M. Johnson, M. Marinkovic, J. Wu, Q. Dai, D.D. Dean, and X.-D. Chen. "Native extracellular matrix preserves mesenchymal stem cell "stemness" and differentiation potential under serum-free culture conditions". *Stem Cell Res. Ther.*, **6**:235, 2015.

[27] A.M. Elbasiony, M.G.A. Saleh, A.O. Ahmed, and A.M. Fathi. "Electrochemical fabrication of TiO_2/TiP_2O_7 and $Ag/TiO_2/TiP_2O_7$ nanocomposites for heavy metal detection and methylene blue dye degradation". *J. Solid State Electrochem*, , 2024.

[28] M. Megha, A. Joy, G. Unnikrishnan, M. Haris, J. Thomas, A. Deepti, P.S.B. Chakrapani, E. Kolanthai, and S. Muthuswamy. "Structural and biological properties of novel vanadium and strontium co-doped HAp for tissue engineering applications". *Ceram. Int.*, **49**.

[29] Z. Xiong, H. Lin, H. Li, B. Zou, B. Xie, Y. Yu, L. He, and T. Chen. "Chiral selenium nanotherapeutics regulates selenoproteins to attenuate glucocorticoid-induced osteoporosis". *Adv. Funct. Mater.*, **33**: 2212970, 2023.

[30] X. Zhou, Y. Qian, L. Chen, T. Li, X. Sun, X. Ma, J. Wang, and C. He. "Flowerbed-inspired biomimetic scaffold with rapid internal tissue infiltration and vascularization capacity for bone repair ". *ACS Nano*, **17**:5140–5156, 2023.

[31] B.K.S. Kumar, M. Jagannatham, B. Venkateswarlu, R. Dumpala, and B.R. Sunil. "Synthesis, characterization, and antimicrobial properties of strontium-substituted hydroxyapatite". *J. Aust. Ceram. Soc.*, **57**:195–204, 2021.

[32] J. Zhuang, N. Li, Y. Zhang, B. Li, H. Wen, X. Zhang, T. Zhang, N. Zhao, and B.Z. Tang. "Esterase-activated theranostic prodrug for dual organelles-targeted imaging and synergetic chemo-photodynamic cancer therapy". *CCS Chem.*, **4**:1028–1043, 2022.

[33] J. Cai, M. Yi, Y. Tan, X. Li, G. Li, Z. Zeng, W. Xiong, and B. Xiang. "Natural product triptolide induces GSDME-mediated pyroptosis in head and neck cancer through suppressing mitochondrial hexokinase-II.". *J. Exp. Clin. Cancer Res.*, **40**:190, 2021.

[34] M. Wypij, T. Jedrzejewski, J. Trzcińska-Wencel, M. Ostrowski, M. Rai, and P. Golinska. "Green synthesized silver nanoparticles: antibacterial and anticancer activities, biocompatibility, and analyses of surface-attached proteins". *Front. Microbiol.*, **12**:632505, 2021.

[35] A. Bernar, J.V. Gebetsberger, M. Bauer, W. Streif, and M. Schirmer. "Optimization of the Alizarin Red S assay by enhancing mineralization of osteoblasts". *Int. J. Mol. Sci.*, **24**:723, 2022.

[36] A. Amirouche, D. Ait-Ali, H. Nouri, L. Boudrahme-Hannou, S. Tliba, A. Ghidouche, and I. Bitam. "TRIzol-based RNA extraction for detection protocol for SARS-CoV-2 of coronavirus disease 2019 ". *New Microbes New Infect.*, **41**:100874, 2021.

[37] X. Zhang, F. Li, Y. Zhou, F. Mao, Y. Lin, S. Shen, Y. Li, S. Zhang, and Q. Sun. "Long noncoding RNA AFAP1-AS1 promotes tumor progression and invasion by regulating the miR-2110/Sp1 axis in triple-negative breast cancer". *Cell Death Dis.*, **12**:627, 2021.

[38] B. Malla, O. Thakali, S. Shrestha, T. Segawa, M. Kitajima, and E. Haramoto. "Application of a high-throughput quantitative PCR system for simultaneous monitoring of SARS-CoV-2 variants and other pathogenic viruses in wastewater". *Sci. Total Environ.*, **853**: 158659, 2022.

[39] S. Takeyari, T. Kubota, Y. Ohata, M. Fujiwara, T. Kitaoka, Y. Taga, K. Mizuno, and K. Ozono. "4-Phenylbutyric acid enhances the mineralization of osteogenesis imperfecta iPSC-derived osteoblasts". *J. Biol. Chem.*, **296**:100027, 2021.

[40] A. Razavi, M. Raei, Y. Hatami, G.S. Chokami, Y. Goudarzi, R. Ghasemian, R. Alizadeh-Navaei, H. Yarmohammadi, M. Soltanipur, M. Tabarestani, R. Valadan, F. Meshkinfam Haghighi, A.K. Tarsi, and B. Razavi. "Evaluation of IFNAR2 and TYK2 transcripts' prognostic role in COVID-19 patients: a retrospective study". *Front. Cell. Infect. Microbiol.*, **14**:1356542, 2024.

[41] E. Cesprini, A. De Iseppi, S. Giovando, E. Tarabra, P. Zanetti, M.and Šket, M. Marangon, and G. Tondi. "Chemical characterization of cherry (Prunus avium) extract in comparison with commercial mimosa and chestnut tannins ". *Wood Sci. Technol.*, **56**: 1455–1473, 2022.

[42] A.G. Abdul Jameel, A.B.S. Alquaity, K.O. Islam, A.A. Pasha, S. Khan, M.A. Nemitallah, and U. Ahmed. "Pyrolysis and oxidation of waste tire oil: analysis of evolved gases". *ACS Omega*, **7**: 21574–21582, 2022.

[43] C.-M. Hu, Q. Yue, F.-G. Zhao, Y. Zhao, B. Pan, L. Bai, X. Wang, and W.-S. Li. "Regioregular and nondestructive graphene functionalization for high-performance electrochromic and supercapacitive devices". *CCS Chem.*, **3**:1872–1883, 2021.

[44] A. Lahchich, P. Álvarez Lloret, J.F. Reynes, and C. Marcos. "Relationships between physicochemical and structural properties of commercial vermiculites". *Materials*, **18**:831, 2025.

[45] Y. Liu, C. Wu, Q. Sun, F. Hu, Q. Pan, J. Sun, Y. Jin, Z. Li, W. Zhang, and Y. Zhao. "Spirobifluorene-based three-dimensional covalent organic frameworks with rigid topological channels as efficient heterogeneous catalyst". *CCS Chem.*, **3**:2418–2427, 2021.

[46] J. Yu, L. Yuan, S. Wang, J. Lan, L. Zheng, C. Xu, J. Chen, L. Wang, Z. Huang, W. Tao, Z. Liu, Z. Chai, J.K. Gibson, and W. Shi. "Phosphonate-decorated covalent organic frameworks for actinide extraction: a breakthrough under highly acidic conditions". *CCS Chem.*, **1**:286–295, 2019.

[47] J.D. Jirsch. "High-frequency oscillations during human focal seizures". *Brain*, **129**:1593–1608, 2006.

[48] H. Zhang. "Preparation and ferroelectric properties of strontium-doped hydroxyapatite ceramics". *Ceram.-Silik.*, **67**:182–188, 2023.

[49] F. Miculescu, A.-C. Mocanu, C.A. Dascălu, A. Maidaniuc, D. Batalu, A. Berbecaru, S.I. Voicu, M. Miculescu, V.K. Thakur, and L.T. Ciocan. "Facile synthesis and characterization of hydroxyapatite particles for high value nanocomposites and biomaterials". *Vacuum*, **146**:614–622, 2017.

[50] M.S. Kothari, A. Aly Hassan, A. Tegenaw, E. Sahle-Demessie, A. El-Dieb, H. El-Hassan, and A. Al-Anazi. "Sustainable synthesis of carbide slag waste derived hydroxyapatite and its application for cationic dye adsorption". *J. Water Process Eng.*, **66**:106001, 2024.

[51] S. Sovova, A. Abalymov, M. Pekar, A.G. Skirtach, and B. Parakhonskiy. "Calcium carbonate particles: synthesis, temperature and time influence on the size, shape, phase, and their impact on cell hydroxyapatite formation ". *J. Mater. Chem. B*, **9**:8308–8320, 2021.

[52] D.J. Hodkin, D.I. Stewart, J.T. Graham, G. Cibin, and I.T. Burke. "Enhanced crystallographic incorporation of strontium(II) ions into calcite via preferential adsorption at obtuse growth steps ". *Cryst. Growth Des.*, **18**:2836–2843, 2018.

[53] L. He, G. Dong, and C. Deng. "Effects of strontium substitution on the phase transformation and crystal structure of calcium phosphate derived by chemical precipitation". *Ceram. Int.*, **42**:1618–1629, 2016.

[54] Ali S. Chitra S. Sudhakar, M.P. "Scrutinizing the effect of rGO-cuttlefish bone hydroxyapatite composite infused carrageenan membrane towards wound reconstruction". *Int. J. Biol. Macromol.*, **262**: 130155, 2024.

[55] M. Wang, X. Ge, Z. Cui, S. Wu, S. Zhu, Y. Liang, Z. Li, and W.W. Lu. "Influences of strontium on the phase composition and lattice structure of biphasic calcium phosphate". *Ceram. Int.*, **47**: 16248–16255, 2021.

[56] M.S. Wong and J.Y. Ying. "Amphiphilic templating of mesostructured zirconium oxide". *Chem. Mater.*, **10**:2067–2077, 1998.

[57] A. Kurzyk, A. Szwed-Georgiou, J. Pagacz, A. Antosik, P. Tymowicz-Grzyb, A. Gerle, P. Szterner, M. Włodarczyk, M.M. Urbaniak, K. Rudnicka, and M. Biernat. "Calcination and ion substitution improve physicochemical and biological properties of nanohydroxyapatite for bone tissue engineering applications". *Sci. Rep.*, **13**:15384, 2023.

[58] E. Yelekli Kirici, S. Angizi, and D. Higgins. "A universal roadmap for quantification of glycerol electrooxidation products using proton nuclear magnetic spectroscopy (1H NMR)". *ACS Catal.*, **14**: 9328–9341, 2024.

[59] S.M. Aksenov, N.V. Chukanov, V.P. Tarasov, D.A. Banaru, S.A. Mackley, A.M. Banaru, S.V. Krivovichev, and P.C. Burns. "The local state of hydrogen atoms and proton transfer in the crystal structure of natural berborite, $Be_2(BO_3)(OH)\cdot H_2O$: low-temperature single crystal X-ray analysis, IR and 1H NMR spectroscopy, and crystal chemistry and structural complexity of beryllium borates". *J. Phys. Chem. Solids*, **189**:111944, 2024.

[60] H.-S. Cho, N.-C. Ha, G. Choi, H.-J. Kim, D. Lee, K.S. Oh, K.S. Kim, W. Lee, K.Y. Choi, and B.-H. Oh. "Crystal structure of Δ5-3-ketosteroid isomerase from Pseudomonas testosteroni in complex with equilenin settles the correct hydrogen bonding scheme for transition state stabilization". *J. Biol. Chem.*, **274**:32863–32868, 1999.

[61] C. Xing, Z. Zhang, Y. Zhang, X. Han, L. Yang, J. Li, X. Wang, P. Martinez, M. Demir, L. Piveteau, P. Florian, J. Arbiol, Y. Guo, J. Llorca, and A. Cabot. "Synergistic effect of surface oxygen vacancies and hydroxyl groups on Cu-doped TiO_2 photocatalyst for hydrogen evolution". *Mater. Today Nano*, **24**:100435, 2023.

[62] Y. Song, X. Meng, M. Bi, and W. Gao. "Effect of hydroxyl groups on the oxygen vacancy and hydrogen-sensitive properties of CeO_2 in different morphologies". *Int. J. Hydrogen Energy*, **47**: 25443–25453, 2022.

[63] D. Rauber, F. Philippi, J. Becker, J. Zapp, B. Morgenstern, B. Kuttich, T. Kraus, R. Hempelmann, P. Hunt, T. Welton, and C.W.M. Kay. "Anion and ether group influence in protic guanidinium ionic liquids". *Phys. Chem. Chem. Phys.*, **25**:6436–6453, 2023.

[64] Z. Zuo, M. Haowei, M. Yarigarravesh, A.H. Assari, M. Tayyebi, M. Tayebi, and B. Hamawandi. "Microstructure, fractography, and mechanical properties of Hardox 500 steel TIG-welded joints by using different filler weld wires". *Materials*, **15**:8196, 2022.

[65] J. Zhu, S. Zhao, J. Luo, W. Niu, J.T. Damron, Z. Zhang, M.A. Rahman, M.A. Arnould, T. Saito, R. Advincula, A.P. Sokolov, B.G. Sumpter, and P.-F. Cao. "A novel dynamic polymer synthesis via chlorinated solvent quenched depolymerization". *CCS Chem.*, **5**: 1841–1853, 2023.

[66] S. Baijnath, I. Kaya, A. Nilsson, R. Shariatgorji, and P.E. Andrén. "Advances in spatial mass spectrometry enable in-depth neuropharmacodynamics". *Trends Pharmacol. Sci.*, **43**:740–753, 2022.

[67] P. Marcus, X. Wang, S. Zanna, A. Seyeux, L. Perrière, M. Laurent-Brocq, I. Guillot, D. Mercier, and V. Maurice. "Enhanced passivity and resistance to pitting of new Cr-Fe-Co-Ni-Mo multi-principal element single-phase alloys". *ECS Meet. Abstr.*, **MA2022-2**:732–732, 2022.

[68] S. Pradeep, A.S. Jain, C. Dharmashekara, S.K. Prasad, N. Akshatha, R. Pruthvish, R.G. Amachawadi, C. Srinivasa, A. Syed, A.M. Elgorban, A.A. Al Kheraif, J. Ortega-Castro, J. Frau, N. Flores-Holguín, C. Shivamallu, S.P. Kollur, and D. Glossman-Mitnik. "Synthesis, computational pharmacokinetics report, conceptual DFT-based calculations and anti-acetylcholinesterase activity of hydroxyapatite nanoparticles derived from Acorus calamus plant extract". *Front. Chem.*, **9**:741037, 2021.

[69] S. Mansingh, S. Subudhi, S. Sultana, G. Swain, and K. Parida. "Cerium-based metal–organic framework nanorods nucleated on CeO_2 nanosheets for photocatalytic N_2 fixation and water oxidation". *ACS Appl. Nano Mater.*, **4**:9635–9652, 2021.

[70] Y. Hao, L. Fang, and Z. Deng. "Solvo-driven dimeric nanoplasmon coupling under DNA direction". *CCS Chem.*, **3**:1359–1367, 2021.

[71] C.U. Nikam, A.P. Birajdar, S.S. Kadam, S.S. Choudhari, V.S. Shinde, S.B. Shelke, R.H. Kadam, and G.H. Kale. "Effect of cation distribution on structural and mechanical properties of Y^{3+} substituted Co-Zn spinel ferrites nanoparticles". *J. Phys. Conf. Ser.*, **2426**:012030, 2023.

[72] A. Abu El-Fadl, A.M. Hassan, and M.A. Kassem. "Tunable cationic distribution and structure-related magnetic and optical properties by Cr^{3+} substitution for Zn^{2+} in nanocrystalline Ni-Zn ferrites". *Results Phys.*, **28**:104622, 2021.

[73] Y.H. Tan, J.A. Davis, K. Fujikawa, N.V. Ganesh, A.V. Demchenko, and K.J. Stine. "Surface area and pore size characteristics of nanoporous gold subjected to thermal, mechanical, or surface modification studied using gas adsorption isotherms, cyclic voltammetry, thermogravimetric analysis, and scanning electron microscopy". *J. Mater. Chem.*, **22**:6733, 2012.

[74] H. Guo, H. Qian, S. Sun, D. Sun, H. Yin, X. Cai, Z. Liu, J. Wu, T. Jiang, and X. Liu. "Hollow mesoporous silica nanoparticles for intracellular delivery of fluorescent dye". *Chem. Cent. J.*, **5**:1, 2011.

[75] A.A. Rabelo, M.C.D. Macedo, D.M.D.A. Melo, C.A. Paskocimas, A.E. Martinelli, and R.M.D. Nascimento. "Synthesis and characterization of $La_{1-x}Sr_xMnO_3 \pm \delta$ powders obtained by the polymeric precursor route". *Mater. Res.*, **14**:91–96, 2011.

[76] N.V. Penkov and N. Penkova. "Key differences of the hydrate shell structures of ATP and Mg ATP revealed by terahertz time-domain spectroscopy and dynamic light scattering". *J. Phys. Chem. B*, **125**: 4375–4382, 2021.

[77] Z. Varga, B. Fehér, D. Kitka, A. Wacha, A. Bóta, S. Berényi, V. Pipich, and J.-L. Fraikin. "Size measurement of extracellular vesicles and synthetic liposomes: The impact of the hydration shell and the protein corona". *Colloids Surf. B*, **192**:111053, 2020.

[78] Q. Zuo, K. Feng, J. Zhong, Y. Mai, and Y. Zhou. "Single-metal-atom polymeric unimolecular micelles for switchable photocatalytic H_2 evolution". *CCS Chem.*, **3**:1963–1971, 2021.

[79] Q. Zhao, H. Yang, L. Tong, R. Jin, and P. Ma. "Understanding the effect of grinding media on the adsorption mechanism of cyanide to chalcopyrite surface by ToF–SIMS, XPS, contact angle, zeta potential and flotation". *Colloids Surf. A*, **644**:128799, 2022.

[80] S. Rahevar, A. Kakati, G. Kumar, J. Sangwai, M. Myers, and A. Al-Yaseri. "Controlled salinity water flooding and zeta potential: insight into a novel enhanced oil recovery mechanism". *Energy Rep.*, **9**:2557–2565, 2023.

[81] R. Wang, K. Yin, M. Ma, T. Zhu, J. Gao, J. Sun, X. Dong, C. Dong, X. Gu, H. Tian, and C. Zhao. "Alkaline phosphatase-initiated sensitive responsiveness of activatable probes to hydrogen sulfide for accurate cancer imaging and differentiation ". *CCS Chem.*, **4**: 3715–3723, 2022.

[82] K. Kostka, S. Hosseini, and M. Epple. "*in-vitro* cell response to strontium/magnesium-doped calcium phosphate nanoparticles ". *Micro*, **3**:156–171, 2023.

[83] A. Anwar, Q. Kanwal, A. Sadiqa, T. Razaq, I.H. Khan, A. Javaid, S. Khan, E. Tag-Eldin, and M. Ouladsmane. "Synthesis and antimicrobial analysis of high surface area strontium-substituted calcium phosphate nanostructures for bone regeneration". *Int. J. Mol. Sci.*, **24**:14527, 2023.

[84] X.-L. Zou, Z.-L. Kang, Y. Li, and H.-J. Ma. "Effect of sodium bicarbonate on solubility, conformation and emulsion properties of pale, soft and exudative meat myofibrillar proteins". *LWT*, **157**: 113097, 2022.

[85] H. Tang, S. Zhang, T. Huang, J. Zhang, and B. Xing. "Mechanisms of the aggregation of graphene oxide at high pH: roles of oxidation debris and metal adsorption". *Environ. Sci. Technol.*, **55**: 14639–14648, 2021.

[86] M.-O. Goebel, J. Bachmann, S.K. Woche, W.R. Fischer, and R. Horton. "Water potential and aggregate size effects on contact angle and surface energy". *Soil Sci. Soc. Am. J.*, **68**:383–393, 2004.

[87] T. Hamieh. "Some irregularities in the evaluation of surface parameters of solid materials by inverse gas chromatography". *Langmuir*, **39**:17059–17070, 2023.

[88] K. Xue, C. Yang, C. Wang, Y. Liu, J. Liu, L. Shi, and C. Zhu. "An exceptional broad-spectrum nanobiocide for multimodal and synergistic inactivation of drug-resistant bacteria". *CCS Chem.*, **4**: 272–285, 2022.

[89] K. Lis, J. Szechyńska, D. Träger, J. Sadlik, K. Niziołek, D. Słota, J. Jampilek, and A. Sobczak-Kupiec. "Hybrid polymer–inorganic materials with hyaluronic acid as controlled antibiotic release systems". *Materials*, **17**:58, 2023.

[90] S. Dehnavi, M. Dadmanesh, N.H. Rouzbahani, M. Karimi, A. Asadirad, M. Gholami, and K. Ghorban. "Mesenchymal stem cell-derived exosome: an interesting nanocarrier to improve allergen-specific intranasal immunotherapy". *Iran. J. Allergy Asthma Immunol*, 2024.

[91] D. Rodríguez-Espinosa, E. Cuadrado-Payán, N. Rico, M. Torra, R.M. Fernández, M. Gómez, L. Morantes, G. Casals, M. Rodriguez-Garcia, F. Maduell, and J.J. Broseta. "Comparative effects of acetate- and citrate-based dialysates on dialysis dose and protein-bound uremic toxins in hemodiafiltration patients: exploring the impact of calcium and magnesium concentrations ". *Toxins*, **16**:426, 2024.

[92] A.R. Boyd, L. Rutledge, L.D. Randolph, I. Mutreja, and B.J. Meenan. "The deposition of strontium-substituted hydroxyapatite coatings ". *J. Mater. Sci. Mater. Med.*, **26**:65, 2015.

[93] E. Boanini, S. Pagani, M. Tschon, K. Rubini, M. Fini, and A. Bigi. "Monetite vs. brushite: different influences on bone cell response modulated by strontium functionalization". *J. Funct. Biomater.*, **13**: 65, 2022.

[94] M.J. Grecula. "CORR insights®: octacalcium phosphate/gelatin composite (OCP/Gel) enhances bone repair in a critical-sized transcortical femoral defect rat model". *Clin. Orthop.*, **480**: 2056–2058, 2022.

[95] M. Etzi Coller Pascuzzi, M. Van Velzen, J.P. Hofmann, and E.J.M. Hensen. "On the stability of Co_3O_4 oxygen evolution electrocatalysts in acid". *ChemCatChem*, **13**:459–467, 2021.

[96] S. Mukesh, P. Joshi, A.K. Bansal, M.C. Kashyap, S.K. Mandal, V. Sathe, and A.T. Sangamwar. "Amorphous salts solid dispersions of celecoxib: enhanced biopharmaceutical performance and physical stability". *Mol. Pharmaceutics*, **18**:2334–2348, 2021.

[97] Z. Gugala. "What's new in musculoskeletal basic science". *J. Bone Jt. Surg.*, **106**:2181–2186, 2024.

[98] C.B. Tovani, T.M. Oliveira, M.P.R. Soares, N. Nassif, S.Y. Fukada, P. Ciancaglini, A. Gloter, and A.P. Ramos. "Strontium calcium phosphate nanotubes as bioinspired building blocks for bone regeneration". *ACS Appl. Mater. Interfaces*, **12**:43422–43434, 2020.

[99] G. Furesi, M. Rauner, and L.C. Hofbauer. "Emerging players in prostate cancer–bone niche communication". *Trends Cancer*, **7**: 112–121, 2021.

[100] Y. Endo, E. Giunta, J. Mroueh, W. McCarthy, and N. Graf. "The application of bioactive materials in bone repair". *Front. Bioeng. Biotechnol*, **12**:1539142, 2025.

[101] Q. Zhao, S. Zhong, and L. Li. "Piezocatalysis for gas generation and disease therapy". *Med. Gas Res.*, **15**:202–203, 2025.

[102] G.S. Stein, J.B. Lian, and T.A. Owen. "Relationship of cell growth to the regulation of tissue-specific gene expression during osteoblast differentiation". *FASEB J.*, **4**:3111–3123, 1990.

[103] T.A. Owen, M. Aronow, V. Shalhoub, L.M. Barone, L. Wilming, M.S. Tassinari, M.B. Kennedy, S. Pockwinse, J.B. Lian, and G.S. Stein. "Progressive development of the rat osteoblast phenotype in vitro: Reciprocal relationships in expression of genes associated with osteoblast proliferation and differentiation during formation of the bone extracellular matrix". *J. Cell. Physiol.*, **143**:420–430, 1990.

[104] D. Bellucci, S. Braccini, F. Chiellini, P. Balasubramanian, A.R. Boccaccini, and V. Cannillo. "Bioactive glasses and glass-ceramics versus hydroxyapatite: Comparison of angiogenic potential and biological responsiveness". *J. Biomed. Mater. Res. A*, **107**:2601–2609, 2019.

[105] M. Li, P. Wan, W. Wang, K. Yang, Y. Zhang, and Y. Han. "Regulation of osteogenesis and osteoclastogenesis by zoledronic acid loaded on biodegradable magnesium-strontium alloy". *Sci. Rep.*, **9**: 933, 2019.

[106] L. Hong, L. Yuan, X. Xu, Y. Ma, L. Meng, J. Wang, N. Zhao, X. Wang, and J. Ma. "Biocompatible nanotube-strontium/polydopamine-arginine-glycine-aspartic acid coating on Ti6Al4V enhances osteogenic properties for biomedical applications". *Microsc. Res. Tech.*, **85**:1518–1526, 2022.

[107] S.-W. Tsai, Y.-W. Hsu, W.-L. Pan, and F.-Y. Hsu. "The effect of strontium-substituted hydroxyapatite nanofibrous matrix on osteoblast proliferation and differentiation". *Membranes*, **11**:624, 2021.

[108] S. Li, L. Zhang, C. Liu, J. Kim, K. Su, T. Chen, L. Zhao, X. Lu, H. Zhang, Y. Cui, X. Cui, F. Yuan, and H. Pan. "Spontaneous immunomodulation and regulation of angiogenesis and osteogenesis by Sr/Cu-borosilicate glass (BSG) bone cement to repair critical bone defects". *Bioact. Mater.*, **23**:101–117, 2023.

[109] Y. Shan, Y. Bai, S. Yang, Q. Zhou, G. Wang, B. Zhu, Y. Zhou, W. Fang, N. Wen, R. He, and L. Zhao. "3D-printed strontium-incorporated β-TCP bioceramic triply periodic minimal surface scaffolds with simultaneous high porosity, enhanced strength, and excellent bioactivity". *J. Adv. Ceram.*, **12**:1671–1684, 2023.

[110] L. Signorini, R. Pistilli, F. Minozzi, M. Gargari, and M. Martelli. "A morphological and immunohistochemical study on the guided bone regeneration technique (GBR) with not resorbable membrane". *Oral Implantol.*, **17**:152–162, 2025.

[111] A.-K. Huber, M. Falk, M. Rohnke, B. Luerßen, L. Gregoratti, M. Amati, and J. Janek. "In situ study of electrochemical activation and surface segregation of the SOFC electrode material La0.75 Sr0.25 Cr0.5 Mn0.5 O3 $\pm$ δ.". *Phys. Chem. Chem. Phys.*, **14**:751–758, 2012.

[112] S. Parvarinezhad, M. Salehi, R. Eshaghi Malekshah, M. Kubicki, and A. Khaleghian. "Synthesis, characterization, spectral studies two new transition metal complexes derived from pyrazolone by theoretical studies, and investigate anti-proliferative activity". *Appl. Organomet. Chem.*, **36**:e6563, 2022.

[113] S. Basu, B. Basu, and P.K. Maiti. "Computational study on strontium ion modified fibronectin-hydroxyapatite interaction". *bioRxiv*, 2021.

[114] J. Rodrigues, M.A. Heinrich, L.M. Teixeira, and J. Prakash. "3D in vitro model (R)evolution: Unveiling tumor–stroma interactions". *Trends Cancer*, **7**:249–264, 2021.

[115] S. Basu, B. Basu, and P.K. Maiti. "A computational study on strontium ion modified hydroxyapatite–fibronectin interactions". *Phys. Chem. Chem. Phys.*, **24**:27989–28002, 2022.

[116] T. Kuwada, M. Shiokawa, Y. Kodama, S. Ota, N. Kakiuchi, Y. Nannya, H. Yamazaki, H. Yoshida, T. Nakamura, S. Matsumoto, Y. Muramoto, S. Yamamoto, Y. Honzawa, K. Kuriyama, K. Okamoto, T. Hirano, H. Okada, S. Marui, Y. Sogabe, T. Morita, T. Matsumori, A. Mima, Y. Nishikawa, T. Ueda, K. Matsumura, N. Uza, T. Chiba, and H. Seno. "Identification of an anti–integrin $\alpha v \beta 6$ autoantibody in patients with ulcerative colitis". *Gastroenterology*, **160**: 2383–2394.e21, 2021.

[117] D.S.H. Lee, Y. Pai, and S. Chang. "Physicochemical characterization of InterOss® and Bio-Oss® anorganic bovine bone grafting material for oral surgery-A comparative study". *Mater. Chem. Phys.*, **146**:99–104, 2014.

[118] M. Bohner. "Resorbable biomaterials as bone graft substitutes". *Mater. Today*, **13**:24–30, 2010.

[119] A. Bigi, E. Boanini, C. Capuccini, and M. Gazzano. "Strontium-substituted hydroxyapatite nanocrystals". *Inorg. Chim. Acta*, **360**: 1009–1016, 2007.

[120] K.J. Joshi, Z.R. Baraiya, and N.M. Shah. "Synthesis of strontium and manganese co-doped hydroxyapatite nanoparticles by ultrasound-supported hydrothermal technique and Taguchi design of experiments for biomedical applications". *Ceram. Int.*, **51**: 3147–3162, 2025.

[121] N.D. Ravi, R. Balu, and T.S. Sampath Kumar. "Strontium-substituted calcium deficient hydroxyapatite nanoparticles: Synthesis, characterization, and antibacterial properties". *J. Am. Ceram. Soc.*, **95**:2700–2708, 2012.

[122] M. Frasnelli, F. Cristofaro, V.M. Sglavo, S. Dirè, E. Callone, R. Ceccato, G. Bruni, A.I. Cornaglia, and L. Visai. "Synthesis and characterization of strontium-substituted hydroxyapatite nanoparticles for bone regeneration ". *Mater. Sci. Eng. C*, **71**:653–662, 2017.

[123] C.J. Harrison, P.V. Hatton, P. Gentile, and C.A. Miller. "Nanoscale strontium-substituted hydroxyapatite pastes and gels for bone tissue regeneration ". *Nanomaterials*, **11**:1611, 2021.

[124] C.R. Akshata, E. Murugan, and G. Harichandran. "Alginate templated synthesis, characterization and in vitro osteogenic evaluation of strontium-substituted hydroxyapatite". *Int. J. Biol. Macromol.*, **252**:126478, 2023.

[125] T. Wu, B. Li, W. Wang, L. Chen, Z. Li, M. Wang, Z. Zha, Z. Lin, H. Xia, and T. Zhang. "Strontium-substituted hydroxyapatite grown on graphene oxide nanosheet-reinforced chitosan scaffold to promote bone regeneration". *Biomater. Sci.*, **8**:4603–4615, 2020.